Bioactive Materials 54 (2025) 201–214

Contents lists available at ScienceDirect

Bioactive Materials

journal homepage: www.keaipublishing.com/en/journals/bioactive-materials

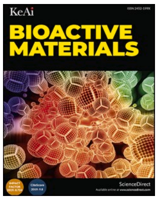

Lithium fine-tunes biodegradation of Zn-based implant to promote osseointegration through immunomodulation

Danni Shen [a,d,j,k,1], Wei Qiao [c,d,1], Xiaoxue Xu [e], Shery L.Y. Chang [f,g], Thomas E. Lockwood [h], Wenting Li [a], Parkarsh Kumar [g], Jie Shen [i], Jun Wu [d], Feihong Liu [d], Kelvin W.K. Yeung [b,d,*], Yufeng Zheng [a,l,**]

[a] *School of Materials Science and Engineering, Peking University, Beijing, 100871, China*
[b] *Department of Orthopedics and Traumatology, The University of Hong Kong, Hong Kong Special Administrative Region of China*
[c] *Applied Oral Sciences and Community Dental Cares, Faculty of Dentistry, The University of Hong Kong, Hong Kong Special Administrative Region of China*
[d] *Shenzhen Key Laboratory for Innovative Technology in Orthopaedic Trauma, Department of Orthopaedics and Traumatology, The University of Hong Kong-Shenzhen Hospital, Shenzhen, 518053, China*
[e] *School of Biomedical Engineering, The University of Technology Sydney, Ultimo, NSW, 2007, Australia*
[f] *Electron Microscope Unit, Mark Wainwright Analytical Centre, University of New South Wales, NSW, 2052, Australia*
[g] *School of Materials Science and Engineering, University of New South Wales, NSW, 2052, Australia*
[h] *Hyphenated Mass Spectrometry Laboratory, The University of Technology Sydney, Ultimo, NSW, 2007, Australia*
[i] *Shenzhen Key Laboratory of Spine Surgery, Department of Spine Surgery, Peking University Shenzhen Hospital, Shenzhen, 518036, China*
[j] *Zhejiang University-University of Edinburgh Institute, Zhejiang University, Haining, 314400, China*
[k] *Department of Sports Medicine of the First Affiliated Hospital, Zhejiang University School of Medicine, Hangzhou, 310058, China*
[l] *International Research Organization for Advanced Science and Technology (IROAST), Kumamoto University, 2-39-2, Kumamoto, 860-8555, Japan*

ARTICLE INFO

Keywords:
Osteoimmunomodulation
Zn-based alloy
Bone regeneration
Osseointegration
Biodegradation

ABSTRACT

The intricate degradation dynamics exhibited by biodegradable alloys significantly influence host responses during the implantation process, posing challenges in achieving stable osseointegration. It is thus critical to tailor the biodegradation profiles of these implants to establish a conductive tissue microenvironment for bone tissue regeneration. In this study, we demonstrate that Zn-Li alloy forms a layer of Li-containing degradation products at the bone-implant interface to accommodate the bone regeneration process. During the early inflammatory phase, the controlled release of lithium ions (Li^+) and zinc ions (Zn^{2+}) from the alloy induces chemokine (C-C motif) ligand 5 (CCL5) production from macrophages, which promotes the recruitment and differentiation of osteoblastic lineage cells. As a protective bone-implant interface is formed subsequently, the active Zn^{2+} release from Zn-Li alloy is suppressed while Li^+ continues to exhibit anti-inflammatory effects and inhibit osteoclastogenesis. Therefore, the presence of Li in Zn-based alloy prevents the prolonged inflammation and fibrous capsulation typically seen in pure Zn implants. Our findings offer valuable insights into the development of novel biodegradable implants aimed at achieving osseointegration through bioadaption.

1. Introduction

Biodegradable Zn-based alloys have attracted widespread attention in the field of biomedical engineering, particularly for orthopedic applications [1–11]. This interest stems from their excellent mechanical properties, moderate biodegradability, and osteogenic bioactivities. The mechanical strength of Zn-based alloys spans a wide range, from below 200 MPa, similar to Mg-based alloys, to over 600 MPa, comparable to stainless steel and titanium alloys, making them suitable for various applications. Our previous studies demonstrated that alloying Zn with magnesium (Mg) or lithium (Li) could significantly improve its mechanical strength to meet the requirements for biodegradable

---

Peer review under the responsibility of editorial board of Bioactive Materials.

* Corresponding author. Department of Orthopedics and Traumatology, The University of Hong Kong, Hong Kong Special Administrative Region of China.

** Corresponding author. School of Materials Science and Engineering, Peking University, Beijing, 100871, China.

E-mail addresses: wkkyeung@hku.hk (K.W.K. Yeung), yfzheng@pku.edu.cn (Y. Zheng).

[1] These authors contribute equally to this work.

https://doi.org/10.1016/j.bioactmat.2025.08.011
Received 3 March 2025; Received in revised form 8 August 2025; Accepted 9 August 2025

orthopedic implants (yield strength >200 MPa, ultimate tensile strength >300 MPa, elongation rate >15–18 %) [12]. Moreover, the degradation rate of Zn-based alloys typically ranges from 0.1 to 0.3 mm/year, which aligns with the degradation rates required for bone fixation implants (0.2–0.5 mm/year), matching the rate of bone healing. Furthermore, Zn^{2+}, the degradation product of Zn-based alloy, are abundant in our body serving as the structural or enzymatic cofactors for approximately 10% of the proteome [13]. We previously reported that Zn^{2+} contributes to bone healing through its immunomodulatory effects at the early inflammatory phase [14,15]. These unique properties make Zn-based alloys a promising candidate for orthopedic applications, especially at load-bearing sites.

Currently, Zn-based alloys have been investigated in various forms, including screws, sutures, pins, and plates, and some have been tested in clinical trials (ChiCTR2100051050) for the treatment of maxillofacial bone fractures. Nevertheless, the alloying of Zn-based implants needs to be carefully tailored, as excessive Zn^{2+} release due to its accelerated degradation would lead to biological toxicity. In our previous attempts to modify Zn-based alloy, we have identified several alloying elements, such as Li and Mg, to be effective in enhancing the mechanical strength and promoting the biocompatibility of the implants [9,10]. For example, due to the low solubility of Li in the Zn matrix, it would precipitate as the eutectic component $LiZn_4$+Zn during the cooling process. When the content of Li in Zn-based alloy is higher than 0.44 wt%, a lamellar structure with interlamellar spacing at several hundred nanometers would form, which refines the grain size, leading to improved strength of the alloy [7,16]. Recently, 3D-printed Zn-0.8Li and Zn-0.8Mg alloys have been shown to achieve optimal osteogenic performance in animal studies [9,10]. However, the early immune responses to these Zn-based alloy and their impacts on subsequent bone regeneration haven't been thoroughly studied *in vivo*.

Bone repair is not solely achieved by osteoblasts and osteoclasts but results from the orchestrated actions of multiple systems. Among these, the immune system and skeletal system are closely related, as they share numerous cytokines, receptors, signaling molecules, and transcription factors [16–20]. Immune cells participate in bone metabolic activities by secreting various regulatory molecules under different physiological or pathological conditions [18]. Orthopedic biomaterials, recognized by the host immune system as foreign bodies upon implantation into bone tissues, would trigger significant immune responses, which will determine the fate of the biomaterials and the outcome of bone regeneration [20]. Compared to biologically inert materials, degradable biomaterials often present a dynamic bone-implant interface with the ongoing degradation processes, which significantly impacts host responses and osseointegration. An excessively active or rapidly changing interface could provoke intense inflammatory responses. For example, magnesium alloys with rapid degradation would cause bone dissolution at the initial phase of implantation [21]. Even traditionally-known inert biomaterials like titanium would release wear debris particles that can trigger local and systemic immune responses [22]. Therefore, a more stable degradation product layer formed on the surface of the degradable implant will better facilitate osteogenesis and biomineralization process [23,24]. We recently developed a Mg-Si-Ca alloy with a self-assembled, hierarchical layered bone-implant interface to achieve bioadaption to the bone [25]. However, whether Zn-based degradable alloys can similarly adapt themselves to bone tissue through this mechanism remains unclear.

In this study, we investigated the degradation behavior of our original Zn-Li alloy system and the host immune response it triggered during the degradation process, as Zn-Li-based alloys exhibit most promising mechanical performance for orthopedic application in our previous researches [26]. We showed that the addition of Li to Zn-based alloy results in the formation of $LiZn_4$ phase, which contributes to the development of Li-containing passive film on the surface of the implant to fine-tune the degradation of the alloy. Compared with pure Zn, Zn-Li alloy better adapts its ion release kinetics to support bone tissue regeneration with a justified degradation mode. Our data indicate that Zn-Li alloy modulates the cytokine secretion from bone macrophages to create a pro-regenerative microenvironment that promotes new bone formation while inhibiting bone resorption. We further identified CCL5 as the key cytokine responsible for the superior osteogenic effect of Zn-Li alloy. Therefore, our findings suggest that Zn-Li alloy represents a new generation of immunomodulatory degradable biomaterials that can be adopted in a variety of clinical applications.

2. Results

2.1. Li fine-tunes the biodegradation behavior of Zn-based alloys

Since the chemical composition and microstructure largely affect the degradation profile of the alloys, we firstly characterized the microstructure of Zn-Li alloys. As depicted by bright field transmission electron microscopy (BF-TEM) morphology imaging and selected area electron diffraction (SAED) patterns (Fig. 1A), the addition of Li introduced $LiZn_4$ intermetallic phase in the Zn matrix, which was also detected by x-ray diffraction (XRD) (Fig. S1A, Supporting Information). The addition of Li has also changed the grain morphology and size distributions, with co-existence of both very elongated grains and more regular hexagonal grains. Overall, Zn-Li alloy has an average grain size of 2.12 μm ± 0.67 μm and an aspect ratio of 1.77 ± 0.34. Moreover, the grain refinement of Zn-Li alloy compared to the pure Zn was observed in the metallographic images and electron backscatter diffraction (EBSD) orientation maps (Fig. S1B, Supporting Information). The presence of Li in the Zn-Li alloy, in agreement with the Zn-Li diffraction results, was further confirmed using electron energy loss spectroscopy (EELS). In order to prevent the migration of Li under the electron beam, we have probed the bulk plasmon signals of Li in the low-loss region of EELS with a low electron beam dose. The bulk plasmon peak of metallic Li has been reported to occur at 7.5 eV [27–29], and the Li-containing metallic compound can exhibit a plasmon energy shift toward lower energies by up to 1 eV (compared to metallic Li) [29]. In comparison to the low loss EELS of Zn with three peaks at 10.0 eV, 14.5 eV and 21.5 eV [30] (shown in bottom-left EELS spectrum in Fig. 1A), our measurement showed an additional peak at 7.1 eV, which was identified as Li in the Li-Zn intermetallic phase.

To examine the biodegradation behavior of the Zn-Li alloy *in vitro*, we conducted a series of electrochemical and immersion tests. As shown in the electrochemical results using stimulated body fluid solution (SBF), Nyquist plots revealed that the impedance loop of Zn-Li alloy is significantly larger than that of pure Zn, indicating that Zn-Li alloy exhibited much higher charge transfer resistance (Fig. 1B). Moreover, in the low-frequency region of Bode plots, Zn-Li alloy showed significantly higher impedance (Fig. 1C). Higher impedance values generally indicated the formation of a dense degradation layer at the surface, which hindered charge transfer and diffusion process. The phase angle of Zn-Li alloy reached a peak value close to 60°, suggesting strong capacitive behavior (Fig. 1D). This could also be attributed to the presence of a passivation film, thereby affecting the charge transfer process. In contrast, pure Zn showed a much lower peak of phase angles, indicating that pure Zn either failed to form a protective layer during degradation or that the protective layer was more easily compromised. These data demonstrated that Zn-Li alloy showed higher corrosion resistance compared with pure Zn and suggested the formation of a passive film at the surface of Zn-Li alloy. To further stimulate the biological degradation process, long-term immersion tests were also conducted in Dulbecco's modified Eagle Medium (DMEM) for 30 days. The ion release profile during 30-day immersion was shown in Fig. 1E and F. Burst release of Li^+ could be observed at the initial stage, and sustained release at a slow pace was shown thereafter. Zn^{2+} release from Zn-Li alloy was less than that from pure Zn, especially at the initial stage, which might prevent the potential toxicity of excessive Zn^{2+} release. The degradation products were carefully characterized by XRD, x-ray photoelectron spectroscopy (XPS),

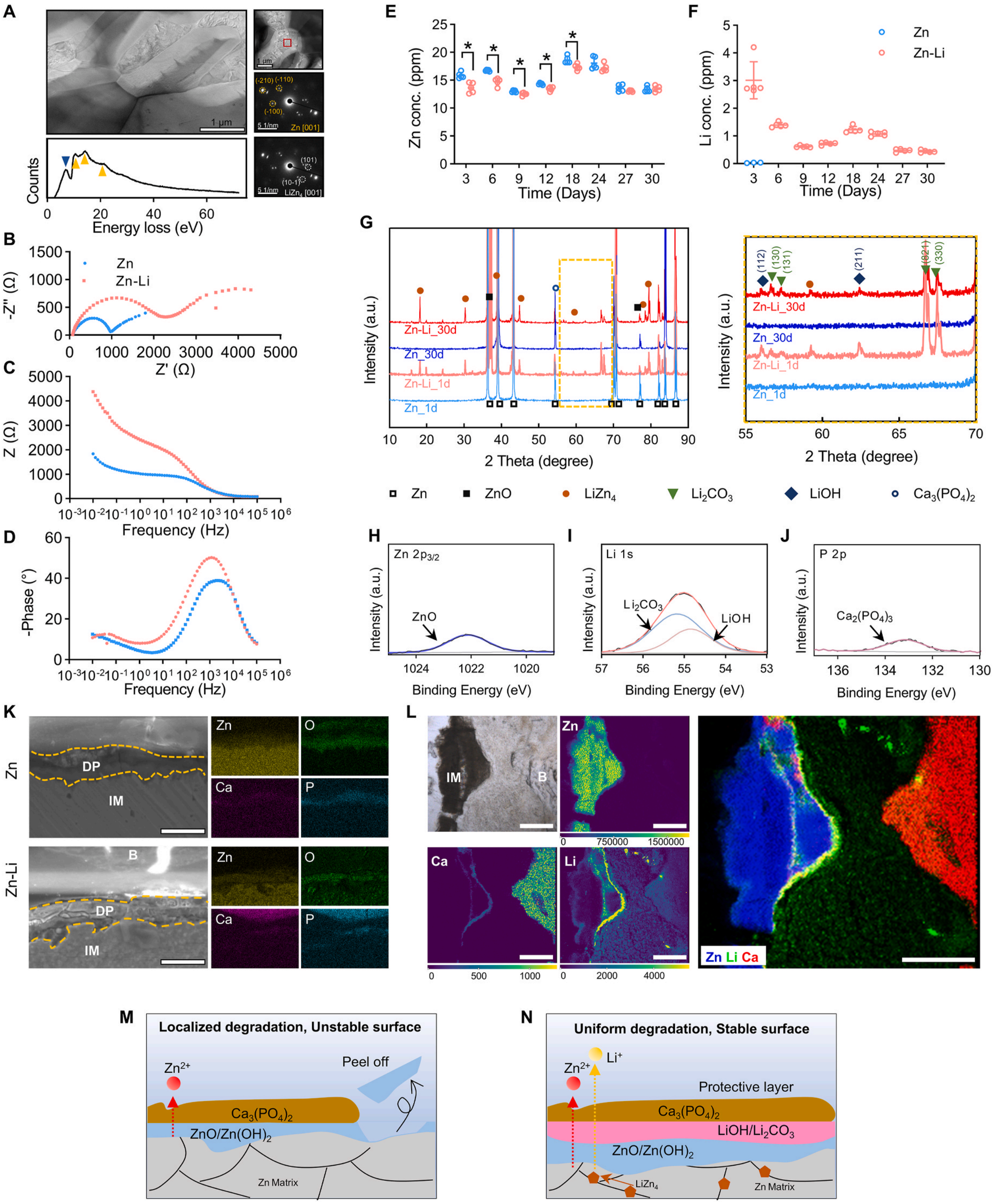

Fig. 1. *In vitro* and *in vivo* degradation behavior of Zn-Li alloy. (A) BF-TEM images, SAED patterns and EELS of Zn-Li alloy. The corresponding SAED patterns of the red boxed region indicated in the BF-TEM image were characterized (right panels, two SAED patterns were assigned to Zn and $LiZn_4$). Arrowheads in yellow represent Zn plasmon peaks, and arrowhead in blue represents Li plasmon peak in EELS (bottom panel). (B–D) Electrochemical results of pure Zn and Zn-Li alloys in SBF, including Nyquist plots (B) and Bode plots (C–D). Z′ is the real part of impedance; Z″ is the imaginary part of impedance; Z is the total impedance. (E–F) Ion release during 30-day immersion in DMEM (n = 5). (G) XRD patterns of materials after immersion in DMEM for 1 day and 30 days. (H–J) XPS analysis of Zn and Zn-Li after immersion in DMEM for 30 days, including Zn $2p_{3/2}$ (H), Li 1s (I), and P 2p (J). (K) Cross-sectional SEM images and corresponding EDS mapping showing the bone–implant interface at week 16 post-operation, yellow dotted line refers to the interface of implant, bone, and degradation products observed under SEM. Zn, scale bars = 10 μm, Zn-Li, scale bars = 25 μm. (L) Element mapping of the bone-implant interface by LA-ICP-MS. Scale bars = 100 μm. (M) Degradation mechanism of pure Zn. (N) Degradation mechanism of Zn-Li alloy. IM: implant; B: bone tissue; DP: degradation products.

and Fourier transform infrared spectroscopy (FTIR) (Fig. 1G–J; Figure S2-S3, Supporting Information). ZnO (2θ = 36.26°, 77.35°) and $Ca_3(PO_4)_2$ (2θ = 54.58°) could be detected in the degradation products of both pure Zn and Zn-Li alloy by XRD. While Li_2CO_3 and LiOH could only be found in the degradation products of Zn-Li alloys, with characteristic peaks at 2θ = 56.71°, 57.95°, 66.76° and 67.42°, corresponding to the (130), (131), (821), and (330) planes of the Li_2CO_3 phase, as well as the peaks at 2θ = 56.03° and 62.26°, corresponding to the (112) and (211) planes of the LiOH phase, respectively. The peaks of Li 1s at 55.2 eV and 54.9 eV in the XPS spectrum further verified the existence of Li_2CO_3 and LiOH (Fig. 1I). Pourbaix diagram of Li-C-H_2O system calculated under physiological conditions also predicted the formation of Li_2CO_3 and LiOH during Zn-Li biodegradation (Fig. S4, Supporting Information).

Next, we further studied the long-term *in vivo* degradation of pure Zn and Zn-Li implants (Φ1.5 × 10 mm) through intramedullary implantation in rat femurs for 16 weeks. We observed that these two implants exhibited quite different degradation behaviors *in vivo*. In general, Zn-Li implant exhibited mild and uniform corrosion *in vivo* with smooth surface morphology during 16-week implantation (Fig. S5A, Supporting Information). In contrast, localized degradation with bulk corrosion products peeled off was observed at the surface of pure Zn. As indicated in the cross-sectional scanning electron microscopy (SEM) images at week 16 post-operation (Fig. 1K), the thickness of the corrosion product layer at the surface of Zn-Li alloy was about 17 μm, which is much higher than that of pure Zn (i.e., ~6 μm). Energy dispersive x-ray spectroscopy (EDS) mapping suggested that the elements within the corrosion products, including Zn, O, Ca, P, and C, are similar between the two groups. Due to the technical limitations of EDS in detecting low-energy X-rays, we employed Laser Ablation Inductively Coupled Plasma Mass Spectrum (LA-ICP-MS) for element Li mapping. Fig. 1L revealed a distinct Li-enriched layer on the outer surface of the degradation products, confirming the presence of the Li-enriched layer *in vivo*. High resolution TEM (HR-TEM) image of the Zn-Li alloy/bone interface region was shown in Fig. S6A–C. The structure transition along the interface was determined using the Fourier diffractogram of the four subregions, suggesting that the interface is transitioned from Zn-Li alloy to crystalline Li_2CO_3 (around 3 nm in subregion 2), followed by poly-crystalline Li_2CO_3 composed of small nanocrystallines (<2 nm in subregion 3) and transitioned into fully amorphous Li_2CO_3 and amorphous $Ca_3(PO4)_2$, which is bone structure (subregion 4). The SAED pattern also showed the exsitence of polycrystalline of Li_2CO_3, Zn and ZnO. The amorphous ring in SAED pattern was highly possible indexed to amorphous Li_2CO_3 (Fig. S6D).

Taken together, our data suggested that the difference in the degradation behavior of pure Zn and Zn-Li alloy may be attributed to the formation of degradation products (Fig. 1M and N). Due to the corrosion potential difference, $LiZn_4$ second phase degraded prior to the Zn matrix and released a considerable amount of Li^+. They reacted with the dissolved O_2 and CO_2 in the tissue fluid, transformed into LiOH and Li_2CO_3,

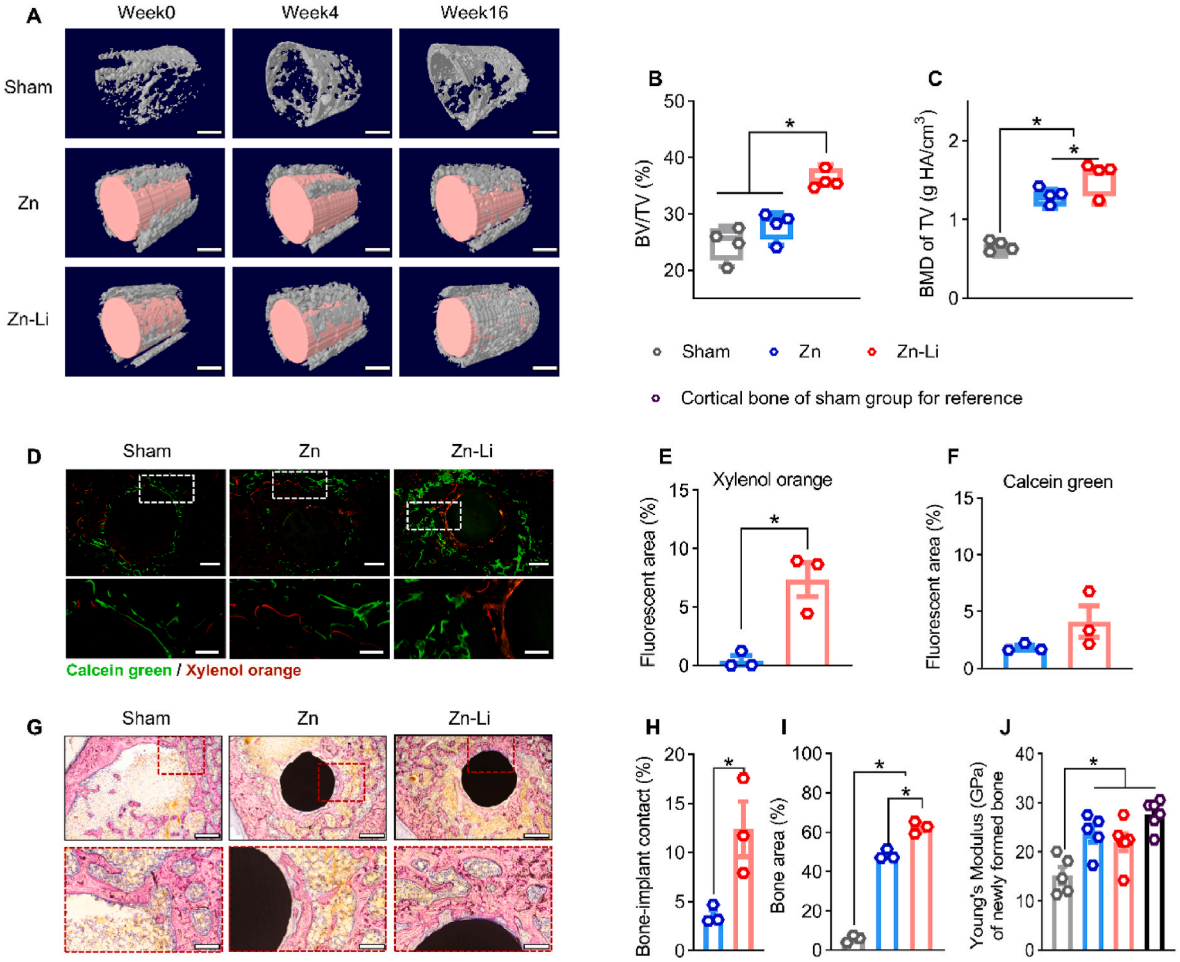

Fig. 2. Zn-Li alloy promotes *in vivo* bone regeneration. (A) Representative reconstructed 3D images of defects in rat femora without implant (Sham, n = 4), with pure Zn (Zn, n = 4) or with Zn-Li implant (Zn-Li, n = 4). Scale bars = 1 mm. (B–C) Corresponding measurements, including BV/TV (B), and BMD of TV (C) of the newly formed bone, showing the regeneration process of bone tissues (n = 4). (D) Representative images of calcein green/xylenol orange labeling for bone regeneration around implants/defects in rat femur. Lower images (scale bars = 200 μm) are high resolution versions of the boxed regions in the upper images (scale bars = 500 μm). (E–F) Corresponding quantitative analysis of fluorescence intensity (n = 3). (G) Representative Giemsa staining showing osseointegration and new bone formation around the implants at week 16 post-operation. Lower images (scale bars = 200 μm) are high resolution versions of the boxed regions in the upper images (scale bars = 500 μm). (H–I) Quantitative analysis of bone-implant contact (H) and bone area around implants/defects (I) (n = 3). (J) Young's modulus of newly formed bone, with matured cortical bone in sham group as reference. Sham, n = 5; Zn, n = 5; Zn-Li, n = 6; cortical bone, n = 6). *$P < 0.05$ by one-way ANOVA with Tukey's *post hoc* (B, C, E, C, H-J).

and deposited at the surface of Zn-Li alloy as a stable protective layer. Although the degradation of $LiZn_4$ would also lead to the release of Zn^{2+}, the diffusion of Zn^{2+} is relatively slower than that of Li^+. Thus, the Zn-containing degradation products deposited at the inner layer, while the Li-containing layer formed at the outer side (Fig. 1L). The presence of $LiOH/Li_2CO_3$ layer contributed to the deposition of Ca^{2+} and PO_4^{3-} from the surrounding bone microenvironment to form a more stable $Ca_3(PO_4)_2$ bone-implant interface, which limited the degradation of the Zn-Li alloy.

2.2. *Zn-Li alloy promoted peri-implant new bone formation and osseointegration*

To evaluate their osteogenic performance, pure Zn and Zn-Li alloy were surgically placed in rat femur as intramedullary implant. The new bone formation around the implant was measured by micro-CT at baseline, post-surgery 4 and 16 weeks. Compared with pure Zn implant, more newly formed bone tissues were observed surrounding the Zn-Li implant (Fig. 2A). However, the bone volume around the defect barely increased from 0 to 16 weeks in the sham group. Quantitative analysis of new bone formation around the defect showed that the bone volume/tissue volume (BV/TV) ratio of the Zn-Li group was 36.44% ± 1.60%, significantly higher than 24.97% ± 3.10% of the sham group and 28.18% ± 2.61% of the Zn group (Fig. 2B). Besides, the bone mineral density (BMD) of tissues surrounding the Zn-Li implant was the highest (1.51 ± 0.21 g HA/cm^3), followed by the Zn group (1.27 ± 0.10 g HA/cm^3) and the sham group (0.61 ± 0.07 g HA/cm^3) (Fig. 2C).

Next, we injected two fluorescent probes (i.e., calcein green and xylenol orange) subcutaneously to visualize calcium deposition around the implants at 1 and 3 weeks after the operation, respectively. The area labeled in green or red was higher in the Zn-Li group than that in the pure Zn group and sham group (Fig. 2D–F, Fig. S7, Supporting Information), indicating a larger amount of newly formed bone at weeks 1 and 3 around the Zn-Li implant compared to other groups. Giemsa staining was conducted to analyze the bone regeneration and osseointegration of the implants at week 16 post-surgery. No significant new bone regeneration was observed in and around the defect in the sham group (Fig. 2G). Despite the presence of bone tissue around pure Zn, a gap between the bone tissue and the implant was observed in the high-magnification image, suggesting poor osseointegration. In contrast, a large amount of bone tissue could be found around the Zn-Li implant, which was in direct contact with the implant. Quantitative analysis showed that the bone-implant contact (BIC) ratio of pure Zn was only 3.63% ± 0.91% while the BIC ratio of Zn-Li alloy reached 12.40%± 4.87% (Fig. 2H). The bone area ratio around Zn-Li implant was 62.42% ± 3.12%, which is significantly higher than that around pure Zn (48.43% ± 2.52%) and sham defect (5.80% ± 1.81%) (Fig. 2I). The Young's modulus of newly formed bone around pure Zn and Zn-Li implant were 23.74 ± 3.97 GPa and 23.52 ± 2.37 GPa, respectively, which was not significantly different from 27.34 ± 3.15 GPa of mature cortical bone (Fig. 2J). However, the Young's modulus of bone tissue around the defect in the sham group was only 15.22 ± 3.82 GPa, significantly lower than that in groups with implants.

The tissue response was further characterized by haematoxylin and eosin (H&E) staining and Masson's trichrome staining (Fig. 3A and B). At 4 weeks post-surgery, we observed that the defect site in the sham

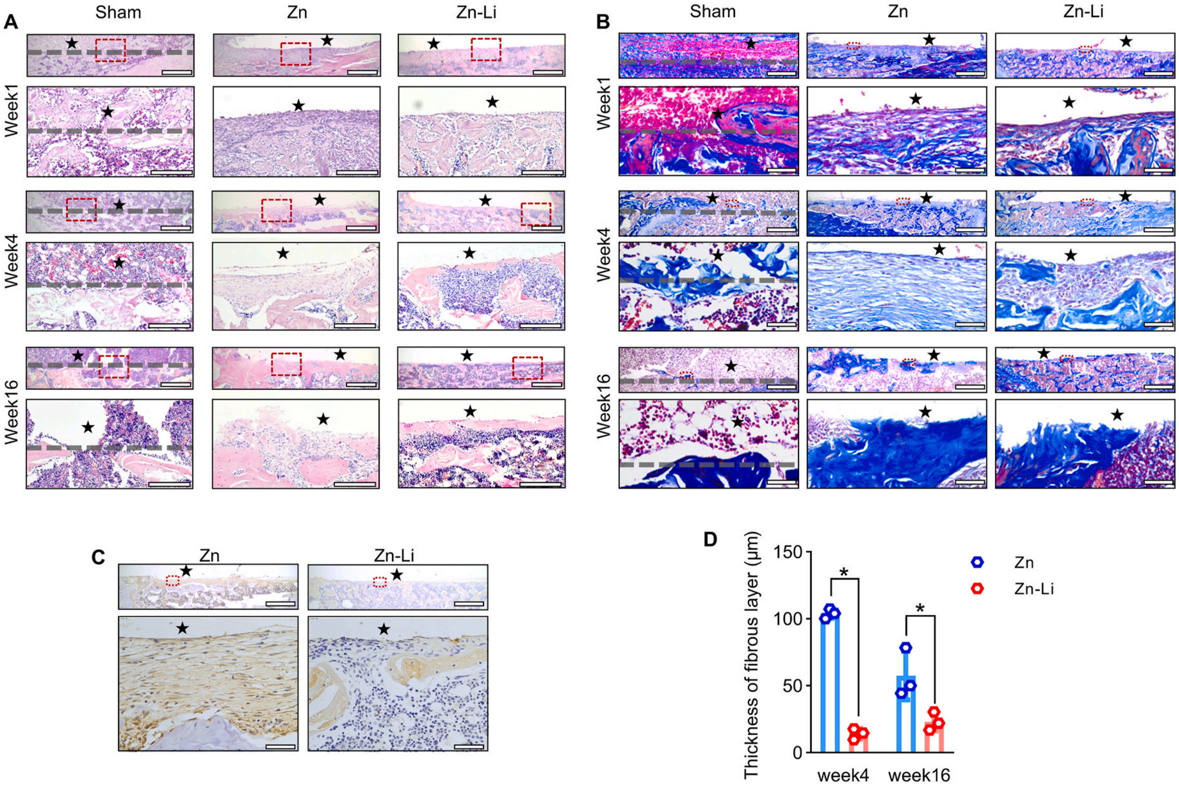

Fig. 3. Osseointegration after implantation. (A) Representative H&E staining images of bone tissues adjacent to defect/implant (marked by ★) at week 1, 4 and 16 post-operation. Lower images (scale bars = 100 μm) are high resolution versions of the boxed regions in the upper images (scale bars = 800 μm). The gray dotted lines in sham group represents the defect margin. (B) Representative Masson's trichrome staining images of bone tissues adjacent to defect/implant (marked by ★) at week 1, 4 and 16 post-operation. Lower images (scale bars = 50 μm) are high resolution versions of the boxed regions in the upper images (scale bars = 800 μm). The gray dotted lines in sham group represents the defect margin. (C) Representative IHC images targeting Collagen I showing the fibrous layer at the interface of implant and bone tissue at week 4 post-operation. Lower images (scale bars = 50 μm) are high resolution versions of the boxed regions in the upper images (scale bars = 800 μm). ★ marks the implant site. (D) Quantification analysis of fibrous layer thickness at week 4 and 16 post-operation (n = 3). *$P < 0.05$ by two-way ANOVA with Tukey's *post hoc*.

group was filled with bone marrow, with little newly formed bone tissue. A thick fibrous layer was observed between pure Zn implant and the bone tissue, while no obvious fibrous encapsulation was observed in the Zn-Li group. At 16 weeks post-surgery, Zn-Li implants were in direct contact with surrounding bone tissue, while a layer of blurred non-bone tissue still existed between Zn implant and bone tissue. Using Collagen I immunohistochemical (IHC) staining, a fibrous layer in the thickness of 103.79 ± 3.56 μm was detected at the interface of Zn implants and bone tissues at week 4 post-surgery, which might be attributed to the excessive inflammation caused by the Zn implant. In comparison, fibrous encapsulation was not evident around Zn-Li implants (Fig. 3C and D).

2.3. Zn-Li alloy modulates macrophage polarization and reshapes the tissue microenvironment

Since the host immune response triggered by the implantation of orthopedic biomaterials has been known as a crucial determinant of the subsequent bone regeneration outcomes, we then compared the immune response elicited by pure Zn and Zn-Li implants. IHC staining of CD68 at week 1 showed no obvious difference in macrophage recruitment between the groups (Fig. 4A). To further investigate the immunomodulatory effects of Zn-Li alloy, we reanalyzed our RNA-sequencing data published previously (GSE262010), which compared the gene expression of macrophages treated with Zn-Li medium extract or culture

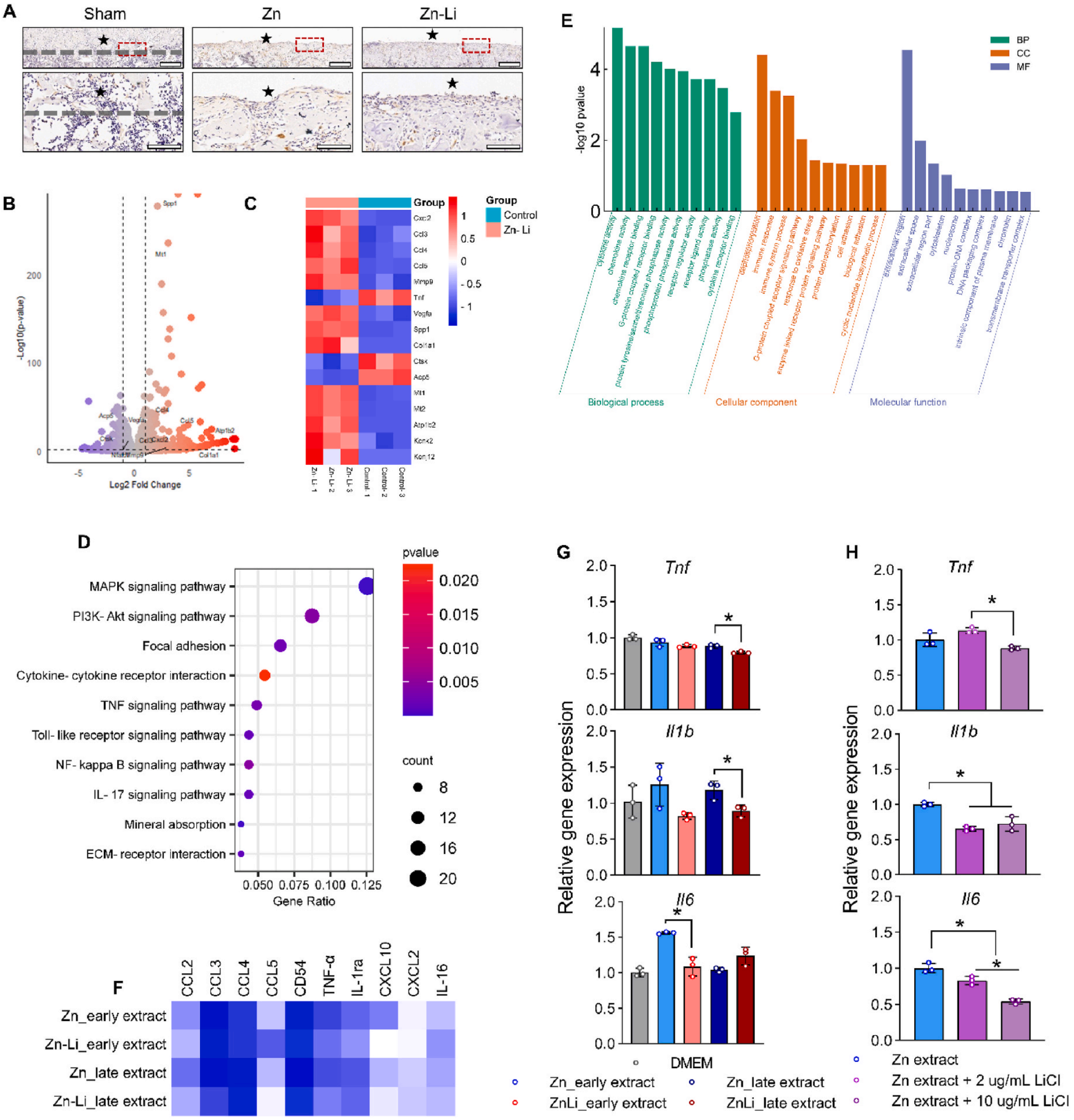

Fig. 4. Immune response and macrophage phenotype regulation caused by Zn-Li alloy. (A) Representative IHC images targeting CD68 showing the accumulation of macrophages in bone tissues adjacent to defect/implant (marked by ★) at week 1 post-operation. Lower images (scale bars = 100 μm) are high resolution versions of the boxed regions in the upper images (scale bars = 400 μm). The gray dotted lines in sham group represents the defect margin. (B) Volcano plot of gene expression compared between RAW264.7 macrophages treated with Zn-Li extract and control medium. (C) Selected gene expression of each sample. (D) KEGG pathway enrichment of differentially expressed genes. (E) GO term analysis of differentially expressed genes. (F) Major cytokines secreted by RAW264.7 cells cultured in different extracts. (G) Expression of pro-inflammatory genes (*Tnf, Il1b, Il6*) by RAW264.7 cells cultured with different extracts (n = 3). (H) Expression of pro-inflammatory genes (*Tnf, Il1b, Il6*) by RAW264.7 cells cultured with Zn extracts supplemented with different concentration of LiCl (n = 3). *$P < 0.05$ by one-way ANOVA with Tukey's *post hoc* (G, H).

medium alone. The volcano plot identified several chemokine genes (e.g., *Cxcl2*, *Ccl3*, *Ccl4*, *Ccl5*) to be upregulated in macrophages treated with the Zn-Li extract (Fig. 4B and C). Besides, genes related to angiogenesis (*Vegfa*) and osteogenesis (*Spp1*, *Col1a1*) were also upregulated by Zn-Li extract. In contrast, the expression of pro-inflammatory genes such as *Tnf*, as well as osteoclastogenesis-related genes, such as *Ctsk* and *Acp5*, were downregulated in the Zn-Li group (Fig. 4C). Moreover, *Atp1b2*, a gene encoding Na^+/K^+ ATPase channel protein, which might play a role in Li^+ transportation [31], was significantly upregulated in the Zn-Li group. The results of gene correlation analysis showed a positive relation between chemokine genes (*Ccl3/4/5*, *Cxcl2/10*) and genes encoding Li^+ transport channels/proteins (*Atp1b2, Kcnk2, Kcnj12*) (Fig. S8, Supporting Information) rather than genes encoding Zn^{2+} transport channels/proteins (*Slc30a*, *Slc39a*, *Mt1/2*, etc.). Kyoto Encyclopedia of Genes and Genomes (KEGG) pathway enrichment (Fig. 4D) and Gene Ontology (GO) term analysis (Fig. 4E) indicated the upregulation of signaling pathways related to energy metabolism, cell activation, and cytokine/chemokine secretion, suggesting the active immune regulatory effect of Zn-Li alloy via chemokine and cytokine interaction.

Considering that Zn-Li extracts significantly altered the phenotype and gene expression in macrophages, we further investigated the supernatant of macrophages cultured with early or late medium extract of pure Zn and Zn-Li alloy. 20 % material extracts were used for the *in vitro* study as we confirmed the cell viability of macrophage wouldn't be compromised at this level of dilution (Fig. S9, Supporting Information). A series of proinflammatory factors (TNF-α, IL-16) and chemokines (e.g. CCL2/3/4/5, CXCL10, CXCL2) that participate in bone fragment removal and preosteoblast homing were determined (Fig. 4F). Compared to pure Zn extract, Zn-Li alloy extract led to decreased levels of CCL2, CCL3, TNF-α, and CXCL10, regardless of whether the extract was from early or late degradation stage. Interestingly, macrophages

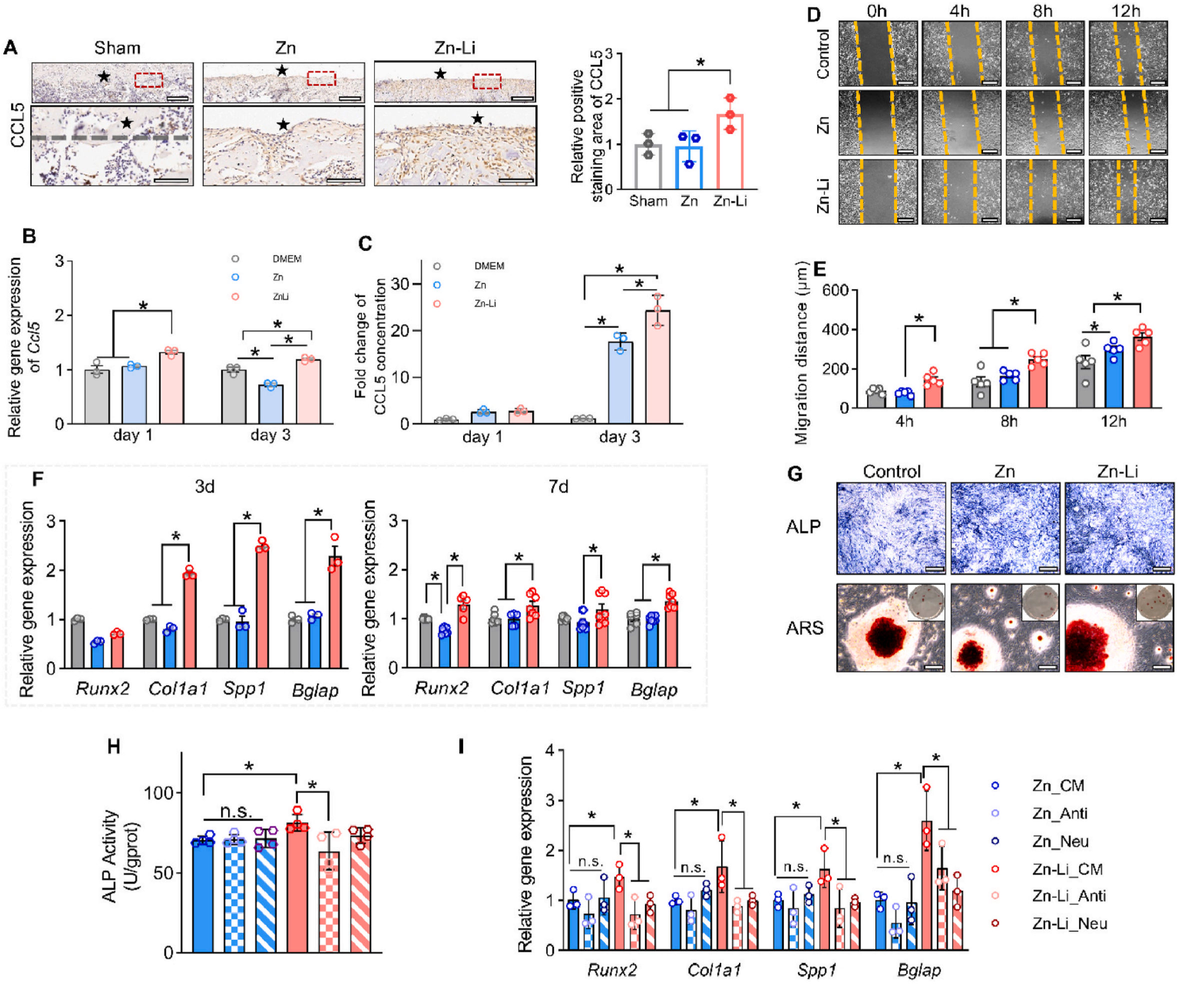

Fig. 5. CCL5 played a vital role in mediating the osteogenic effect of Zn-Li alloy. (A) Representative IHC images targeting CCL5 in bone tissues adjacent to defect/implant (marked by ★) at week 1 post-operation and corresponding quantification showing the effect of Zn-Li alloy on CCL5 expression (n = 3). Lower images (scale bars = 100 μm) are high resolution versions of the boxed regions in the upper images (scale bars = 400 μm). The gray dotted lines in sham group represents the defect margin. (B) *Ccl5* gene expression in RAW264.7 cells cultured with extracts for 1 and 3 days (n = 3), showing the stimulatory effect of Zn-Li alloy extract on *Ccl5* gene expression. (C) ELISA analysis of the supernatant of RAW264.7 cells after culture with extracts for 1 and 3 days (n = 3), showing the stimulatory effect of Zn-Li alloy extract on CCL5 secretion. (D) Wound closure results of MC3T3-E1 cells cultured with conditioned medium, showing promotion of Zn-Li conditioned medium to cell migration. The yellow dashed lines represent the front line of cell migration. (E) Migration distance of MC3T3-E1 cells cultured in conditional medium (n = 5). (F) Osteogenic gene expression of MC3T3-E1 cells cultured in conditioned medium for 7 days (n = 3). (G) ALP and alizarin red staining (ARS) of MC3T3-E1 cells cultured in conditioned medium (supplemented osteogenic induction agent) for 7 days and 21 days, representatively. (H, I) ALP activity (H, n = 4) and osteogenic gene expression (I, n = 3) of MC3T3-E1 cells cultured in conditioned medium with (Neu) or without CCL5 neutralizing antibody (CM), or with CCR1/3/5 inhibition agent (Anti). $^*P < 0.05$ by Student's t-test (Zn_CM v.s. Zn-Li_CM in H, I), one-way ANOVA with Tukey's *post hoc* (A), one way-ANOVA with Dunnett's *post hoc* (Zn_CM, Zn_Anti, Zn_Neu in H, Zn-Li_CM, Zn-Li_Anti, Zn-Li_Neu in H), two-way ANOVA with Tukey's *post hoc* (B, C, E), and two-way ANOVA with Dunnett's *post hoc* (Zn_CM, Zn_Anti, Zn_Neu in I, Zn-Li_CM, Zn-Li_Anti, Zn-Li_Neu in I).

treated with early extracts of Zn-Li alloy showed higher concentrations of CCL5 in the supernatant compared to those treated with pure Zn, while in the case of late extracts of pure Zn and Zn-Li alloy, they exhibit opposite effects on CCL5. Using real-time quantitative polymerase chain reaction (RT-qPCR), we confirmed the effects of Zn-Li alloy extract on downregulating pro-inflammatory genes, such as *Tnf, Il1b, and Il6* (Fig. 4G). This unique immunomodulatory effect of Zn-Li alloy is likely due to the presence of Li^+ in the supernatant as the addition of Li^+ to pure Zn extract replicated the anti-inflammatory effects of Zn-Li alloy (Fig. 4H). Notably, this effect may be further amplified by the

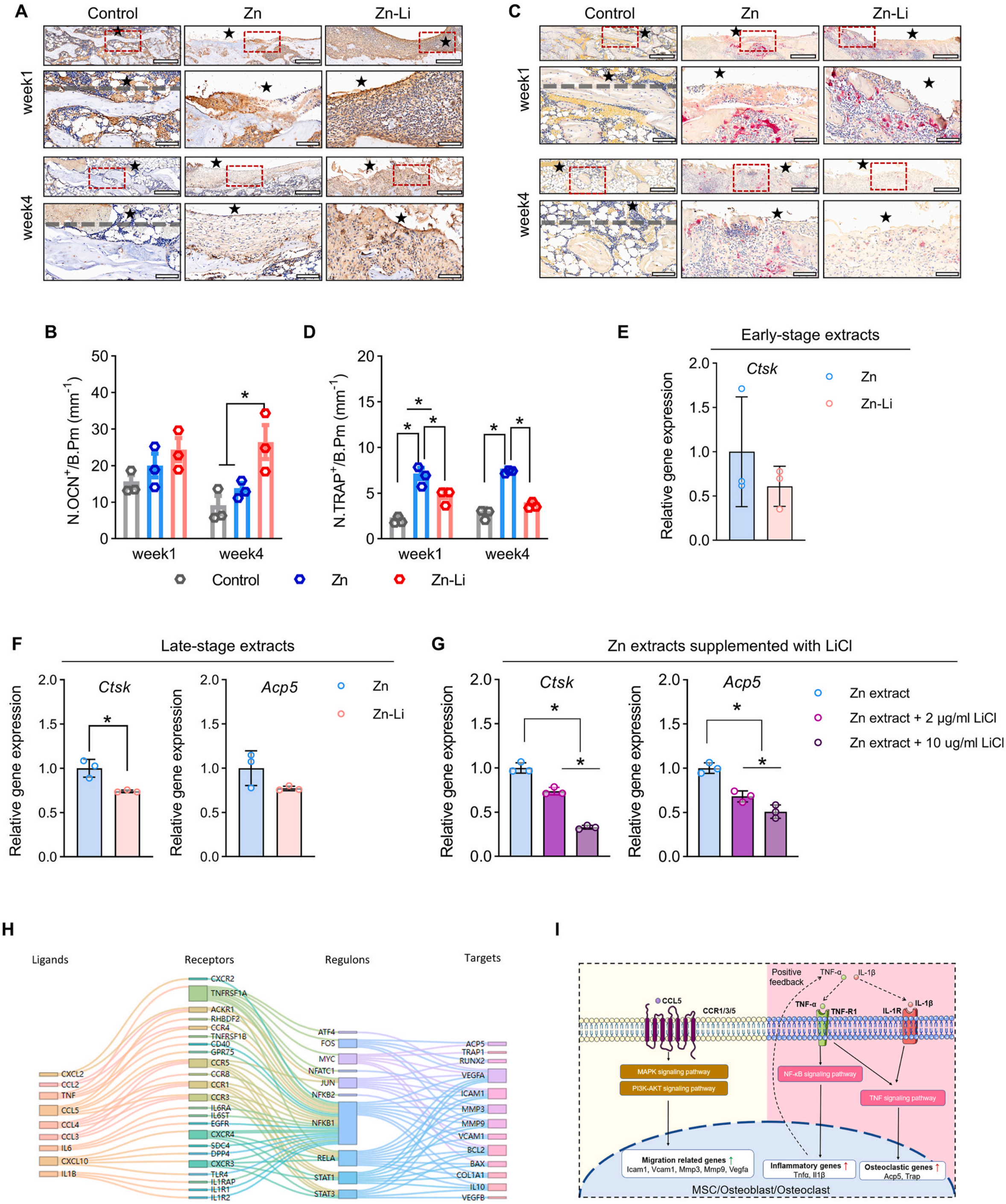

Fig. 6. Zn-Li alloy affects both bone formation and bone resorption process *in vivo*. (A) Representative IHC images showing the expression of OCN. Lower images (scale bars = 100 μm) are high-resolution versions of the boxed regions in the upper images (scale bars = 400 μm). ★ represents defect/implant site. The gray dotted lines in sham group represents the defect margin. (B) Quantification of OCN-positive cells (n = 3). (C) Representative Trap-staining images showing osteoclast activity at different times after surgery. Lower images (scale bars = 100 μm) are high-resolution versions of the boxed regions in the upper images (scale bars = 400 μm). ★ represents defect/implant site. The gray dotted lines in sham group represents the defect margin. (D) Quantification of Trap-positive cells (n = 3). (E, F) Osteoclastic-related gene expression in RAW264.7 cells cultured with early (E) and late (F) extracts, n = 3. (G) Osteoclastic-related gene expression in RAW264.7 cells cultured with Zn extract supplemented with different concentration of LiCl, n = 3. (H) Sankey plot of ligand-receptor-regulon-target axis using database of CellTalkDB and DoRothEA. (I) Impact of CCL5, TNF-α and IL-1β on the target cells (MSC/Osteoblast/Osteoclast). *$P < 0.05$ by two-way ANOVA with Tukey's *post hoc* (B, D), by Student's Student's t-test (E, F) one-way ANOVA with Tukey's *post hoc* (G).

simultaneous reduction of Zn^{2+} release compared with pure Zn. The orthogonal experiments revealed that while elevated Zn^{2+} alone upregulated pro-inflammatory/fibrotic genes (e.g., *Il6*, *Col1a1*), the combined modulation of Li^{+} and Zn^{2+} in the alloy led to a synergistic suppression of these markers (Fig. S10, Supporting Information).

2.4. The vital role of CCL5 in mediating the osteogenic effect of Zn-Li alloy

Among the cytokines/chemokines regulated by Zn-Li alloy, we identified CCL5 to be consistently upregulated by Zn-Li alloy at both transcriptomic and protein levels. Therefore, we further examined the effect of Zn-Li alloy on CCL5 both *in vivo* and *in vitro*. We first showed the number of CCL5 positive cells around Zn-Li implant was significantly higher compared to that in the sham group and pure Zn group (Fig. 5A). RT-qPCR and enzyme-linked immunosorbent assay (ELISA) data both demonstrated that Zn-Li extracts at the early stage of degradation upregulated the production of CCL5 (Fig. 5B and C). The conditioned medium from Zn-Li alloy-treated macrophage, which contained a higher level of CCL5 than that from pure Zn-treated macrophage, significantly promoted the migration and proliferation of preosteoblasts (Fig. 5D and E; and Fig. S11, Supporting Information). Moreover, we showed that Zn-Li alloy-treated macrophage-derived conditioned medium significantly upregulated the expression of early osteogenic marker genes such as *Runx2* and *Col1a1*, as well as late osteogenic marker genes such as *Spp1* and *Bglap* (Fig. 5F). Meanwhile, the alkaline phosphatase (ALP) activity and mineral deposition were also higher in preosteoblasts treated with Zn-Li alloy conditioned medium (Fig. 5G). Nevertheless, Zn-Li extract alone was not able to enhance the osteogenic activity of preosteoblasts (Fig. S12, Supporting Information). Additionally, when CCL5 in the conditioned medium was neutralized by the antibody or the CCL5 receptors were blocked, the superior osteogenic effect of the Zn-Li alloy was abolished (Fig. 5H and I). This suggested that CCL5 is a critical osteogenic factor in the Zn-Li alloy-induced immune microenvironment.

2.5. Li^{+} released from Zn-Li implant inhibits bone resorption

Bone regeneration involves coordinated actions of both bone formation and bone resorption. To investigate the effect of Zn and Zn-Li on bone regeneration more comprehensively, we performed IHC staining of osteocalcin (OCN) and tartrate-resistant acid phosphatase (TRAP) osteoclast staining to evaluate the influences of pure Zn and Zn-Li implants on these two processes. At week 4 post-surgery, the number of OCN-positive cells in the bone tissue around Zn-Li implants was significantly higher than that of the other two groups, indicating more active bone formation around Zn-Li implant (Fig. 6A and B). By contrast, the number of TRAP-positive cells in Zn-Li group was much less than that in the Zn group, suggesting more suppressed bone resorption around Zn-Li implant (Fig. 6C and D). Compared with pure Zn, Zn-Li extracts tended to downregulate the expression of several osteoclastogenic genes, including *Ctsk,* and *Acp5* (Fig. 6E and F). The inhibitory effect of Zn-Li extracts can be reproduced by directly supplementing pure Zn extract with Li^{+} (Fig. 6G). Therefore, the inhibitory effect of Zn-Li alloy on osteoclasts may be largely attributed to the release of Li^{+}.

Then, we further explored the potential mechanisms responsible for the immunomodulatory effect of Zn-Li alloy and its influence on bone remodeling using Sankey plot of ligand-receptor-transcript factor-target axis (Fig. 6H). The degradation of Zn-Li alloy triggered the production of chemokine CCL5 from macrophages. They act on osteoblasts through binding to their receptors CCR1/3/5 at the cell membrane, resulting in the upregulation of genes mainly related to cell migration (*Icam1*, *Vcam1*) through the activation of MAPK and PI3K-AKT signaling pathways, thereby leading to the recruitment and differentiation of osteoblast lineage cells. By contrast, excessive Zn^{2+} release from pure Zn provokes a variety of pro-inflammatory cytokines (e.g., TNF-α and IL-1β) from macrophages, which prolongs the inflammation and upregulate osteoclastic activity mainly through the TNF signaling pathway and NF-κB signaling pathway (Fig. 6I).

3. Discussion

The biodegradation of implants would shape the immune microenvironment, thereby modulating the bone regeneration process. We showed that Li incorporation contributes to the presence of the $LiZn_4$ phases within α-Zn matrix. Previous studies have reported that lamellar morphology of the α-Zn and $LiZn_4$ eutectic structure refines the grain size of the materials to alleviate the localized corrosion [7,32]. Compared with Zn (standard potential −0.76 V vs. SHE), Li is more active (standard potential −3.04 V vs. SHE), therefore, $LiZn_4$ second phase degraded prior to the Zn matrix. Upon the degradation of $LiZn_4$, released Li^{+} accumulates at the bone-implant interface and reacts with H_2O to form LiOH and H_2. LiOH then further reacts with CO_2 to form Li_2CO_3, contributing to a layer of Li-containing protective corrosion products to suppress the degradation of the alloy (Equations 1 and 2). Previous studies on Zn-based alloys with similar composition consistently show that the corrosion resistance improves with the increase of Li content [32,33]. Meanwhile, released Zn^{2+} following the degradation of the Zn matrix also reacts with H_2O and dissolved O_2 in tissues to form $Zn(OH)_2$, part of which dehydrates into ZnO (Equations 3 and 4). In addition to the corrosion products mentioned above, the deposition of Ca^{2+} and PO_4^{3-} from the surrounding bone microenvironment also contributes to the formation of $Ca_3(PO_4)_2$ at the bone-implant interface, but this occurs only at a relatively later stage of bone tissue regeneration.

$$2\mathrm{Li} + 2H_2O \rightarrow 2LiOH(s) + H_2\uparrow \qquad \text{(Equation 1)}$$

$$2\mathrm{LiOH(s)} + CO_2 \rightarrow Li_2CO_3(s) + H_2O \qquad \text{(Equation 2)}$$

$$2\mathrm{Zn(s)} + O_2 + 2H_2O \rightarrow 2Zn(OH)_2(s) \qquad \text{(Equation 3)}$$

$$Zn(OH)_2(s) \rightarrow \mathrm{ZnO(s)} + H_2O \qquad \text{(Equation 4)}$$

The standard formation enthalpies of the corrosion products LiOH, Li_2CO_3, $Zn(OH)_2$, and ZnO are −484.93 kJ/mol, −1216.04 kJ/mol, −645.4 kJ/mol and −384.3 kJ/mol, respectively. Theoretically, the stability of corrosion products is $Li_2CO_3 > Zn(OH)_2 > LiOH > ZnO$. Therefore, the Li-containing corrosion layer on the surface of Zn-Li alloy is more stable than the degradation products on the surface of Zn, which contains ZnO/ZnOH only. Consequently, the degradation products of Zn-Li alloy provide better protection to the implant to prevent excessive Zn^{2+} release before the formation of $Ca_3(PO_4)_2$ at the later stage.

Li is a trace element that can be found in our body and it has various biological functions. As the active component of lithium carbonate, an FDA-approved medication for bipolar disorder for more than 60 years [34], Li has been studied for its effects on bone homeostasis and is increasingly used in the modification of orthopedic biomaterials [35–40]. While the anti-inflammatory effects of Li are recognized [41], its involvement in bone tissue regeneration remains incompletely understood. In this study, we demonstrated that the controlled release of Li^{+} from the Zn-Li alloy at the initial degradation stage downregulated the expression of pro-inflammatory cytokines, including *Tnf, Il1b,* and *Il6*, in macrophages, providing a favorable immune microenvironment for subsequent bone repair. Critically, this effect might be amplified by the simultaneous reduction of Zn^{2+} release compared with pure Zn, as excessive Zn^{2+} release not only induces cytotoxicity but also augments inflammatory response [42], suppressing osteogenesis. Our orthogonal experiments further revealed that while elevated Zn^{2+} alone upregulated pro-inflammatory/fibrotic genes (e.g., *Il6*, *Col1a1)*, the combined Li^{+}/Zn^{2+} modulation in the alloy exhibited synergistic suppression of these markers, suggesting their cooperative anti-inflammatory effect (Fig. S10, Supporting Information). Moreover, we demonstrated that Li^{+} released from Zn-Li alloy directly inhibits osteoclastogenic differentiation and suppresses bone resorption. Without the formation of

Li-containing corrosion products as a protective bone-implant interface, sustained Zn^{2+} release from pure Zn leads to prolonged inflammation around the implants, resulting in bone destruction and fibrous encapsulation. Additionally, Li may directly affect the biomineralization process. Indeed, Li-containing biomaterials have been shown to contribute to better biomineralization compared to their counterparts without Li [43–45]. It has been reported that Li^{+} can directly activate CaSR and stimulate calcium release from the endoplasmic reticulum and mitochondria to form matrix vehicles. These matrix vehicles containing high concentration of Ca and P can then be secreted to ECM to initiate biomineralization around implants [46]. Future studies should explore whether this mechanism contributes to Zn-Li alloy's osteogenicity, alongside investigations into Li^{+}/Zn^{2+} crosstalk (e.g., using ion-selective chelators or omics profiling) to dissect their individual versus synergistic roles.

CCL5, a chemokine present during tissue injury, has been known to be involved in various stages of bone regeneration [47–49]. For example, it was found to promote the homing of bone marrow mesenchymal stem cells and endothelial stem cells, which is conducive to early osteogenesis and angiogenesis [47,50]. Besides, studies have shown that CCL5 is directly involved in the regulation of osteogenesis, and the depletion of CCL5 leads to impaired bone formation. Downregulation of endogenous CCL5 expression could impair bone formation, while overexpression of CCL5 enhances the osteogenic activities [48,49]. The effects of CCL5 on osteoclastogenesis remain controversial, with studies reporting both stimulatory [51,52] and inhibitory [48,53] effects on osteoclast functions. This indicates that CCL5 may be a double-edged sword during bone regeneration. In this study, we noticed that the distinct degradation behavior of Zn-Li alloy at early and late stages of bone regeneration allows an intriguing transitional upregulation and later inhibition of CCL5. Thus, the immune microenvironment created by Zn-Li alloy can promote the homing and osteogenic activity of osteoblasts at the early inflammatory stage while preventing the activation of osteoclasts during the bone remodeling stage. CCL5 achieves its biological functions by binding to several receptors on the cell membrane, with CCR1, CCR3, and CCR5 playing a major role [54]. Our data showing that the blockage of CCR1/3/5 abolished the osteogenic effect of Zn-Li alloys suggests CCL5 to be the major mediator for Zn-Li alloy-induced osteogenesis.

As emerging biodegradable alloys, Zn-based alloys require precise modification to achieve optimal properties before successful translation into practical applications. Zn is an essential element in physiological processes, and it can promote osteoblastic differentiation at appropriate concentrations. However, excessive Zn^{2+} release may induce toxicity and chronic inflammation. Therefore, controlling the degradation of zinc alloys and managing the release profile of Zn^{2+} is a crucial safety consideration in the development of Zn alloys. Various alloying elements has distinct effects on the degradation behavior of Zn-based alloys. Based on previous studies, the incorporation of Fe [55], Ag, Cu [56], and Sr accelerates degradation, while the addition of Mg and Mn has minimal effect on degradation rate [57]. In contrast, Zn alloys containing element Li significantly inhibit degradation, partially due to the protective effect of the Li-rich degradation product layer, which reduces excessive Zn^{2+} release. Negative correlation between Zn^{2+} concentration and cell viability was observed. Zn-Fe and Zn-Cu alloys accelerate degradation and increase cytotoxicity compared with pure Zn, while Zn-Li alloys significantly improve cell compatibility. Other metal ions would also release accompanying Zn^{2+} during alloy degradation, which may interact synergistically or antagonistically with Zn^{2+}, thus affecting biocompatibility. For instance, Zn-Mg alloys, although not significantly reducing Zn^{2+} release, may reduce Zn^{2+} transport into cells due to competitive binding with Mg^{2+} to ion transport proteins [58–60], thereby decreasing toxicity. Further research could focus on these interactions and aim to decouple the function of each metal ion, to more comprehensively unravel the underlying mechanisms. Pure Zn was chosen as the control group in this study to minimize confounding variables, and we tried to explore the effect of Li incorporation on the immunomodulatory performance of the alloy, providing insights for the future development of Zn-Li-based alloys as orthopedic materials.

While we believe our results provide strong evidence supporting our findings in this study, we acknowledge that some limitations still need to be considered. For instance, in our initial micro-CT quantitative analysis, a sample size of four revealed substantial differences between the experimental and control groups, while the intra-group variations were minimal. Therefore, we proceeded with a smaller sample size for the subsequent experiments, which yielded consistent and reliable results to support the robustness of our findings. Nonetheless, we acknowledge that the sample size could be increased to further improve the reliability and generalizability of our results in our future studies. Another issue may arise from the method for the quantification of histological specimens. We quantified the fluorescent signals from multiple regions on histological sections and then conducted statistical analysis based on the mean value from each sample. While this approach is currently widely used in histological studies, we believe quantification using new 3D reconstruction-based methods would offer a more accurate and reliable measurement, which should be considered in our future work.

4. Conclusion

This study elucidated how the biodegradation of Zn-Li alloy is fine-tuned by Li alloying to achieve superior osseointegration by modulating the innate immune response. The formation of Li_2CO_3 at the bone-implant interface better aligns the degradation pattern of the implant with the bone regeneration process. The controlled release of Li^{+} and Zn^{2+} fosters a more pro-regenerative microenvironment by exerting immunomodulatory effects on macrophages and inhibitory regulation on osteoclasts directly. Specifically, our study pinpointed CCL5 as the pivotal mediator driving the osteoimmunomodulatory effects of Zn-Li alloy. Therefore, the findings of this study provide valuable insights into the tissue immune responses to degradable alloy, thereby stimulating the advancement of novel degradable implants for orthopedic applications.

5. Materials and methods

Material preparation: Pure Zn and Zn-Li alloys were fabricated from raw materials, Zn (99.99 %) and Zn-6wt.%Li alloy, by Hunan Rare Earth Metal Material Research Institute in China. After casting, the materials were homogenized at 350°C for 48 h and were followed by water quenching. Then, the ingots were hot extruded at 260°C with an extrusion ratio of 36:1. Alloys were cut into disks ($\Phi 10 \times 1$ mm) for *in vitro* tests. All the samples were ground to 2000 grit with SiC paper, followed by ultrasonical cleaning sequentially in acetone, absolute ethanol, and distilled water. For *in vivo* implantation, alloys were cut into rods ($\Phi 1.5 \times 10$ mm), ground to 2000 grit and ultrasonically cleaned. Prior to implantation, rods were sterilized by UV-irradiation for 4 h. The composition of pure Zn and Zn-0.4Li alloy were listed in Table S1, Supporting Information).

Microstructure characterization: The TEM samples were prepared by Ar plasma focus ion beam (Hydra PFIB, ThermoFisher Scientific, USA). Prior to TEM observation, the samples were further milled using low-energy (600 eV) Ar ions (NanoMill, Fischione) to remove surface oxidation layers. Bright-field TEM images and SAED patterns were acquired using JEM-F200 (JEOL, Japan), operated at 200 kV. EELS (GIF Continuum, Gatan, USA) was carried out using GrandArm dual aberration corrected TEM (JEOL, Japan) equipped with cold field emission source and Gatan continuum energy filter with direct electron detector, K3. To minimize electron beam-induced damage to the samples, low electron fluencies were used to acquire the EELS spectra.

Electrochemical tests: The electrochemical tests were carried out in SBF (Yuanye, R24030, China; detailed information of ion concentration in SBF was shown in Table S2, Supporting Information) using an electrochemical workstation (Autolab, Metrohm, Switzerland). A three-electrode cell system was used. Platinum electrode and saturated calomel electrode were chosen as counter electrode and reference electrode, respectively. Materials tested were designated as the working electrode. The open circuit potential (OCP) was measured for 3600 s. Potentiodynamic polarization was conducted ranging from −500 mV to 500 mV (vs. OCP) at a scan rate of 1 mV/s. Corrosion potential (E_{corr}) and corrosion current density (i_{corr}) were calculated from Tafel extrapolation. Electrochemical impedance spectroscopy (EIS) was also measured by applying 10 mV perturbation with frequency ranging from 10^5 Hz to 10^{-2} Hz.

In vitro ion release profile: Specimens were immersed in DMEM (Gibco, USA) containing 10% fetal bovine serum (FBS, Gibco, USA) with a ratio of 1.25 cm^2/mL at 37°C in a humidified atmosphere with 5% CO_2. At designated time points (day 3, 6, 9, 12, 18, 24, 27 and 30), the culture medium was replenished with fresh medium. The concentrations of Zn^{2+} and Li^+ in the medium were measured using Inductively Coupled Plasma-Mass Spectrometry (ICP-MS, DCR II, Sciex, USA). In brief, by measuring the standard solutions of Zn and Li at various concentrations, a calibration curve was created to relate the signal intensity of each element to its exact concentration. Each sample was measured three times, and five samples were tested at each time point for each group.

In vitro biodegradation morphology and composition: The surface morphology of pure Zn and Zn-Li alloy after immersion in culture medium was observed using SEM (Quattro S, ThermoFisher Scientific, USA). The element distribution of Zn, O, Ca, P, and C on the surface and cross-section were analyzed using EDS (AZtecOne, HITACHI, Japan) mapping. The composition of the degradation products was examined using XRD (D/MAX 240, Rigaku, Japan), XPS (AXIS Supra, Kratos Analytical Ltd., UK), and FTIR (Nicolet iS50, ThermoFisher Scientific, USA).

Animal surgery: Thirty female Sprague-Dawley (SD) rats (Ages:11–13 weeks old) with a weight of 250–300 g were chosen for experiments. Prior to the surgery, rats were anaesthetized via intraperitoneal injection of ketamine hydrochloride (67 mg/kg; Alfamine, Alfasan International B.V., Holland) and xylazine hydrochloride (6 mg/kg; Alfamine, Alfasan International B.V., Holland). After hair shaving, a hand drill was employed to intramedullary drill through the marrow cavity to create tunnel defects on both sides at the distal femur with the size of Φ1.5 × 10 mm. In pure Zn and Zn-Li groups, material rods were implanted into the prepared tunnel defects in the left femur, while leaving the tunnel defect empty in the right femur. In the control groups, tunnel defects on both sides were left empty. Then the wound was sutured layer by layer and 1 mg/kg terramycin and 0.5 kg/mg ketoprofen were subcutaneously administered for antibiotic prophylaxis and analgesic, respectively. The rats were euthanized at post-surgery 1, 4, and 16 weeks.

Micro-CT analysis: New bone formation around the implanted pure Zn or Zn-Li implants was monitored by the micro-CT machine (SKYSCAN 1076, Skyscan Company, Belgium) at various post-operation time points (0, 4, and 16 weeks). A resolution of 17.33 μm, a voltage of 88 kV, and an amperage of 100 μA were selected to obtain the CT images. Phantoms containing rods with standard densities of 0.25 and 0.75 g/cm^3 were scanned for calibration. BV/TV, as well as the BMD surrounding the implant were systemically analyzed by the CTAn software (Skyscan Company, Belgium). The 3D models of new bone formation were reconstructed by the CTVol software (Skyscan Company, Belgium).

Fluorochrome labeling: Two fluorochrome labels were injected sequentially to evaluate the dynamic bone regeneration and remodeling process within the defects and around the implants. Calcein green (5 mg/kg, Sigma-Aldrich) was subcutaneously injected 1 week after the surgery, while xylenol orange (90 mg/kg, Sigma-Aldrich) was injected 3 weeks after the surgery. The fluorochrome labels were visualized under a fluorescence microscopy (Niko ECL IPSE 80i, Japan) from the non-decalcified femur sections that were detailed in the following parts. The intensity of fluorescence was analyzed by ImageJ software (NIH, USA). Three different sections of each sample were imaged and the average fluorescence area ratio was calculated.

Histological analysis: After euthanasia, rat femora were collected and fixed in 4% paraformaldehyde solution (Biosharp, China). For non-decalcified sections, the samples were dehydrated with 70%, 95%, and 100% ethanol solutions for 72 h each, respectively. Xylene was used as an intermediate solvent for another 4-day immersion. Methyl methacrylate (MMA) solutions (MMA I, MMA II, and MMA III, detailed information was shown in Table S3, in Supplementary Materials) were adopted sequentially for embedding the samples. Finally, the embedded samples were cut into slices with a thickness of 200 μm by a microtome (EXAKT, Germany) and micro-ground to a thickness of 50–70 μm. Giemsa solution (Giemsa(v): DI water(v) = 1:4, MERCK, Germany) was used to stain the newly formed bony tissue around the implants/defect. The images of stained femur slides were observed by an optical microscope (ECLIPSE 80i, Nikon, Japan). The bone area surrounding the implants/defects was measured according to the Giemsa staining images. Three samples were measured for each group, and three different sections of each sample were analyzed. For decalcified sections, the samples were decalcified with 12.5% ethylenediaminetetraacetic acid (EDTA, Sigma-Aldrich, USA) for 6 weeks. After retrieval of the implants, the specimens were then dehydrated in ethanol, embedded in paraffin, and cut into 5 μm-thick sections using a rotary microtome (RM215, Leica Microsystems, Germany). H&E staining (Beyotime, China), TRAP staining (Sigma-Aldrich, USA), and Masson's trichrome staining (Beyotime, China) were performed in selected slides from each sample following manufacturer's instructions. Images were captured using a polarizing microscopy (Eclipse VL100POL, Nikon, Japan). The fibrous layer and bone tissue were distinguished based on morphology and color in Masson's staining images. The thickness of the fibrous layer was measured at five different fields on each section using Image J (NIH, USA), and three samples were measured for each group.

Immunohistochemistry analysis: For immunohistochemical staining, the dewaxed slides were treated with citrate (pH = 6, CST, USA) for antigen retrieval and 3% H_2O_2 for the elimination of endogenous peroxidase activity. After blocking with Animal-Free Blocking Solution (CST, USA), the slides were incubated with primary antibody overnight at 4°C. The primary antibodies used in this study include rabbit-anti-rat CD68, rabbit-anti-rat CCL5, rabbit-anti-rat OCN, and rabbit-anti-rat Collagen I (Abcam, USA). The slides were then incubated with goat anti-rabbit secondary antibody (Abcam, USA) and visualized using Diaminobenzidine (DAB) staining kit (CST, USA) following the manufacturer's instruction. Three different fields were selected from each sample for analysis to increase the representativeness of the data and reduce errors that might arise from relying on a single field of view.

Young's modulus measurement: The unstained non-decalcified sections were employed to measure Young's moduli of newly formed bone by a Nano Indenter (G200, MTS System Corporation, USA). During the tests, applied maximum load and drift rate were maintained at 10 mN and 1.2 nm/s, respectively. Six samples in each group were measured for statistical significance.

Alloy extract preparation: Extracts were prepared using DMEM culture medium (Gibco, USA) with a surface area to medium volume ratio of 1.25 cm^2/mL at 37°C in a humidified atmosphere of 5% CO_2 for 24 h. The supernatant was withdrawn, centrifuged, filtered using 0.22-μm filter, and reserved at 4°C for use.

LA-ICP-MS analysis: LA-ICP-MS was conducted for elemental distribution analysis on the interface of the bone and the implant. LA-ICP-MS analyses were performed on a laser ablation system (Elemental Scientific Lasers Image BIO266 Kennelec, Mitcham, Australia) coupled to an Agilent 7900 series ICP-MS (Mulgrave, Australia). Images of Zn, Li, Ca, and P were collected at a 2 μm spot size, scan speed of 10 μm/s, and repetition rate of 200 Hz. The ICP-MS acquisition time was 0.1 s. Data processing was performed in Pew2 version 1.6.1 [61].

In vivo biodegradation morphology and composition characterization: The TEM lamella of the non-decalcified sample was prepared using the

Helios 5 FIB-SEM under cryogenic condition. TEM imaging and selected area diffraction was carried out using JEOL F200 operated at 200 kV, at lower-dose condition to avoid damage to the bone and its interfaces.

Cell culture: RAW264.7 cells (a murine macrophage cell line, National Collection of Authentical Cell Cultures, China) and MC3T3-E1 cells (a murine pre-osteoblast cell line, National Collection of Authentical Cell Cultures, China) were used in this study. Both cells were maintained in the DMEM cell culture medium (Gibco, USA) containing 10% FBS (Gibco, USA) and 1% (v/v) penicillin/streptomycin (Gibco, USA) at 37°C with 5% CO_2 humidified atmosphere. Regarding the passage procedure, the RAW264.7 cells were dislodged by gently passing a cell scraper over the surface of the flask after the cells reaching around 80% confluence, which were then seeded to new flasks. Cell passages of MC3T3-E1 pre-osteoblasts occurred when they proliferated to more than 80–90% confluence. The culture medium was carefully discarded and the cells were washed using PBS (Gibco, USA) for 3 times before adding trypsin (Gibco, USA) for cell detachment. The detached cells were collected, centrifuged, and seeded to new flasks.

Extracts preparation for cell experiments: The extracts were obtained by immersing the Zn or Zn-Li alloy in DMEM culture medium with 10% FBS at 37°C. The 'early extract' refers to the extract collected on day 3, while the 'late extract' refers to the extract collected on day 30, as mentioned previously. Except for the explicit mention of 'early extracts' and 'late extracts', all the extracts we used for cell experiments were prepared by extraction for 24 h. As an exception, extracts used in the migration assay were prepared by DMEM culture medium without FBS. The concentrations of Zn^{2+} and Li^{+} in the extracts were measured using Inductively Coupled Plasma-Mass Spectrometry (ICP-MS, DCR II, Sciex, USA). Each sample was measured three times.

Cytokine release: RAW264.7 cells were cultured with alloy extracts for 72 h and the supernatants were collected for cytokine evaluation. The cytokines produced by RAW264.7 cells after the stimulation by different extracts were determined by Proteome Profiler antibody arrays (R&D System, USA) following the manufacturer's instructions. The concentration of CCL5 was further confirmed by specific ELISA kits (R&D system, USA). Two replicate wells were used for each sample in the ELISA assay.

Conditioned medium preparation: RAW264.7 cells were cultured by different alloy extracts for 72 h. The supernatants were collected and mixed 1:1 (v/v) with corresponding fresh extracts. The conditioned medium was stored at 4°C and used within 1 month.

Cell proliferation assay: The effect of Zn and Zn-Li alloy on the proliferation of RAW264.7 and MC3T3-E1 cells was assessed using a Cell Counting Kit-8 (CCK-8, Dojindo, Japan). Cells were cultured either by complete culture medium or alloy extracts in 96-well plates. At designated time points, the culture medium was replaced by fresh serum-free medium containing 10% CCK-8. After incubation at 37°C for 1–4 h, the optical density (OD) value at the wavelength of 450 nm was measured using a microplate spectrophotometer (Thermo Scientific, USA).

Migration assay: MC3T3-E1 cells were seeded in 12-well plates at a proper density. After the confluence of the cells, a scratch was made using the pipette head. After washing off the cell debris using PBS three times, the cells were treated with the conditioned medium. The extracts and conditioned medium used for the migration assay were prepared using DMEM medium without FBS to minimize the effect of proliferation. Images showing the width of the scratch were obtained using a microscope (CKX53, OLYMPUS, Japan) and analyzed using ImageJ software. Five fields were captured per group and analyzed as technical replicates.

Osteogenesis differentiation assay: Osteogenic supplements with 10 mM β-glycerol phosphate (Sigma, USA), 50 μM L-ascorbic acid (Sigma, USA), and 100 nM Dexamethasone (Sigma, USA) were added to full culture medium or alloy extracts to culture MC3T3-E1 cells. The osteogenic medium was refreshed every two days.

ALP assay: The ALP activity was adopted for characterization of osteogenic activity of MC3T3-E1 cells. After cultured by osteogenic medium for 7 days, MC3T3-E1 cells were rinsed with PBS three times and lysed with the lysis buffer solution (Beyotime, China) at 4°C for 30 min. The cell lysates were centrifugated by 13000 g centrifugation at 4°C for 5 min. 30 μL supernatant was transferred into a 96-well plate followed by addition of working reagent in the ALP reagents kit (Nanjing Jiancheng, China). The absorbance was measured by the micro-plate spectrophotometer (Thermo Scientific, USA) at 520 nm and ALP activity of MC3T3-E1 cells was normalized to the total protein level via a BioRad Protein Assay (Bio-Rad, USA).

Mineralization assay: Alizarin Red staining was used to study the formation of calcium nodules during osteogenic induction. At the designated time points, MC3T3-E1 cells were washed by PBS and fixed by 4% paraformaldehyde solution, and the calcium nodules were stained with Alizarin Red S solution (Sigma, USA) for 5 min. After thorough washing, the sample was air-dried before photo taking.

RT-qPCR assay: The total RNA of the cells was extracted and purified using RNAprep pure Cell/Bacteria Kit (Tiangen, China) following the manufacturer's instructions. For the reverse transcript, complementary DNA was synthesized using RevertAid First Strand cDNA Synthesis Kit (ThermoFisher Scientific, USA) following the manufacturer's instructions. The primers used in the RT-qPCR assay were synthesized by Invitrogen (ThermoFisher Scientific, USA) based on the sequences retrieved from Primer Bank (http://pga.mgh.harvard.edu/primerbank/, Table S4, Supporting Information). QuantiNova SYBR Green PCR Kit (Qiagen, Germany) was used for the amplification and detection of cDNA targets on a Real-time PCR system (LC480, Roche, Switzerland). The mean cycle-threshold (Ct) value of each target gene was normalized to the house-keeping gene *Gapdh*. The results were presented in fold change using the ΔΔCt method. Each sample was analyzed in triplicate for each target gene to minimize measurement variation.

CCL5 neutralization and blockage: For the neutralization of CCL5, CCL5 antibody (ab9783, Abcam, USA) was added into the conditioned medium in the final concentration of 1 μg/mL. For the inhibition of CCR1/3/5 (CCL5 receptors) activity, cells were pretreated with CCR antagonist (J 113863, SB 328437, Maraviro; R&D Systems, USA) for 3 h, washed with PBS, and subjected to the other assays.

Bioinformatic analysis: The RNA sequencing analysis was conducted based on the data published previously (GSE262010 [7]). GO term analysis and KEGG pathway enrichment analyses were performed based on the differentially expressed genes (DEGs). The ligand-receptor-transcription factor-target interaction analysis was performed based on CellTalkDB and DoRothEA databases. Figures were created using the free online platform of http://www.bioinformatics.com.cn.

Statistical analysis: The data were evaluated by Student's t-test, one-way analysis of variance (ANOVA) with Tukey's *post hoc*, one-way ANOVA with Dunnett's *post hoc*, two-way ANOVA with Tukey's *post hoc*, and two-way ANOVA with Dunnett's *post hoc* multiple comparison test. The data were presented as mean ± standard deviation and a difference of $^{*}P < 0.05$ was considered significant.

CRediT authorship contribution statement

Danni Shen: Writing – review & editing, Writing – original draft, Visualization, Investigation, Funding acquisition, Conceptualization. **Wei Qiao:** Writing – review & editing, Writing – original draft, Visualization, Investigation, Funding acquisition, Conceptualization. **Xiaoxue Xu:** Visualization, Investigation. **Shery L.Y. Chang:** Visualization, Investigation. **Thomas E. Lockwood:** Visualization, Investigation. **Wenting Li:** Investigation. **Parkarsh Kumar:** Investigation. **Jie Shen:** Investigation. **Jun Wu:** Investigation. **Feihong Liu:** Investigation. **Kelvin W.K. Yeung:** Writing – review & editing, Supervision, Resources, Project administration, Funding acquisition, Conceptualization. **Yufeng Zheng:** Writing – review & editing, Supervision, Resources, Project administration, Funding acquisition, Conceptualization.

Ethics approval and consent to participate

The surgical procedures and post-operative care protocol were licensed and strictly implemented according to the requirements of the Ethics Committee of the University of Hong Kong (CULATR NO.4053-16) and the Licensing Office of the Department of Health of the Hong Kong Government.

Declaration of competing interests

Yufeng Zheng is an editor-in-chief for Bioactive Materials and was not involved in the editorial review or the decision to publish this article. Kelvin W. K. Yeung and Xiaoxue Xu are associate editors for Bioactive Materials and were not involved in the editorial review or the decision to publish this article, Wei Qiao is an early career editorial board member for Bioactive Materials and were not involved in the editorial review or the decision to publish this article. All authors declare that there are no competing interests.

Acknowledgements

We sincerely thank the staff members at the Centre for PanorOmic Sciences of Li Ka Shing Faculty of Medicine and the Centre for Comparative Medicine Research, the University of Hong Kong for providing a harmonious working environment. We thank Hongtao Yang of Beihang University (Beijing, China) for the metallographic test. Electron microscope facilities at Elecron Microscope Unit (EMU), UNSW, are gratefully acknowledge. We also thank Dr. Charlie Kong for his asistance in preparing the TEM samples. This work is supported by National Natural Science Foundation of China/Research Grants Council Joint Research Scheme (N_HKU721/23 to W.Q. and NSFC-RGC 5231101024 to Y.Z.), General Research Fund of the Research Grants Council (17207719, 1711322, K.W.K.Y. and 17118425, W.Q.), Hong Kong Innovation Technology Fund (ITS/256/22, W.Q.), Health and Medical Research Fund (21200592, 22210832, 23220925, K.W.K.Y., 09201466, W.Q.), Collaborative Research Fund of the Research Grants Council (C5044-21G, K.W.K.Y., C7003-22Y, W.Q.), National Key R&D Program of China (2023YFB3810203, K.W.K.Y), National Natural Science Foundation of China (U22A20121, 51931001, Y.Z., 82201124, W. Q., 32301098, D.S.), Beijing Natural Science Foundation Haidian Original Innovation Joint Fund (L212014, Y.Z.), Shenzhen Science and Technology Innovation Committee Projects (SGDX20220530111405 038 to W.Q., JCYJ20210324120009026, JCYJ20210324120012034 to K.W.W.Y.), Guangdong Basic and Applied Basic Research Foundation (2023A1515011963, W.Q.).

Appendix A. Supplementary data

Supplementary data to this article can be found online at https://doi.org/10.1016/j.bioactmat.2025.08.011.

References

[1] X. Liu, J. Sun, F. Zhou, Y. Yang, R. Chang, K. Qiu, Z. Pu, L. Li, Y. Zheng, Micro-alloying with Mn in Zn–Mg alloy for future biodegradable metals application, Mater. Des. 94 (2016) 95–104, https://doi.org/10.1016/j.matdes.2015.12.128.

[2] S. Zhao, C. McNamara, P. Bowen, N. Verhun, J.P. Braykovich, J. Goldman, J. W. Drelich, Structural characteristics and in vitro biodegradation of a novel Zn-Li alloy prepared by induction melting and hot rolling, Metall. Mater. Trans. 48 (2017) 1204–1215, https://doi.org/10.1007/s11661-016-3901-0.

[3] P. Li, C. Schille, E. Schweizer, F. Rupp, A. Heiss, C. Legner, U.E. Klotz, J. Geis-Gerstorfer, L. Scheideler, Mechanical characteristics, in vitro degradation, cytotoxicity, and antibacterial evaluation of Zn-4.0Ag alloy as a biodegradable material, Int. J. Mol. Sci. 19 (2018) 755, https://doi.org/10.3390/ijms19030755.

[4] P. Li, W. Zhang, J. Dai, A.B. Xepapadeas, E. Schweizer, D. Alexander, L. Scheideler, C. Zhou, H. Zhang, G. Wan, J. Geis-Gerstorfer, Investigation of zinccopper alloys as potential materials for craniomaxillofacial osteosynthesis implants, Mater. Sci. Eng. C 103 (2019) 109826, https://doi.org/10.1016/j.msec.2019.109826.

[5] B. Jia, H. Yang, Y. Han, Z. Zhang, X. Qu, Y. Zhuang, Q. Wu, Y. Zheng, K. Dai, In vitro and in vivo studies of Zn-Mn biodegradable metals designed for orthopedic applications, Acta Biomater. 108 (2020) 358–372, https://doi.org/10.1016/j.actbio.2020.03.009.

[6] B. Jia, H. Yang, Z. Zhang, X. Qu, X. Jia, Q. Wu, Y. Han, Y. Zheng, K. Dai, Biodegradable Zn–Sr alloy for bone regeneration in rat femoral condyle defect model: in vitro and in vivo studies, Bioact. Mater. 6 (2021) 1588–1604, https://doi.org/10.1016/j.bioactmat.2020.11.007.

[7] H. Yang, X. Qu, M. Wang, H. Cheng, B. Jia, J. Nie, K. Dai, Y. Zheng, Zn-0.4Li alloy shows great potential for the fixation and healing of bone fractures at load-bearing sites, Chem. Eng. J. 417 (2021) 129317, https://doi.org/10.1016/j.cej.2021.129317.

[8] H. Kabir, K. Munir, C. Wen, Y. Li, Recent research and progress of biodegradable zinc alloys and composites for biomedical applications: biomechanical and biocorrosion perspectives, Bioact. Mater. 6 (2021) 836–879, https://doi.org/10.1016/j.bioactmat.2020.09.013.

[9] J. Xu, G. Bao, B. Jia, M. Wang, P. Wen, T. Kan, S. Zhang, A. Liu, H. Tang, H. Yang, B. Yue, K. Dai, Y. Zheng, X. Qu, An adaptive biodegradable zinc alloy with bidirectional regulation of bone homeostasis for treating fractures and aged bone defects, Bioact. Mater. 38 (2024) 207–224, https://doi.org/10.1016/j.bioactmat.2024.04.027.

[10] S. Li, H. Yang, X. Qu, Y. Qin, A. Liu, G. Bao, H. Huang, C. Sun, J. Dai, J. Tan, J. Shi, Y. Guan, W. Pan, X. Gu, B. Jia, P. Wen, X. Wang, Y. Zheng, Multiscale architecture design of 3D printed biodegradable Zn-based porous scaffolds for immunomodulatory osteogenesis, Nat. Commun. 15 (2024) 3131, https://doi.org/10.1038/s41467-024-47189-5.

[11] C. Wu, F. Lin, H. Liu, M.H. Pelletier, M. Lloyd, W.R. Walsh, J.-F. Nie, Stronger and coarser-grained biodegradable zinc alloys, Nature 638 (2025) 684–689, https://doi.org/10.1038/s41586-024-08415-8.

[12] H. Yang, B. Jia, Z. Zhang, X. Qu, G. Li, W. Lin, D. Zhu, K. Dai, Y. Zheng, Alloying design of biodegradable zinc as promising bone implants for load-bearing applications, Nat. Commun. 11 (2020) 401, https://doi.org/10.1038/s41467-019-14153-7.

[13] A. Weiss, C.C. Murdoch, K.A. Edmonds, M.R. Jordan, A.J. Monteith, Y.R. Perera, A. M. Rodríguez Nassif, A.M. Petoletti, W.N. Beavers, M.J. Munneke, S.L. Drury, E. S. Krystofiak, K. Thalluri, H. Wu, A.R.S. Kruse, R.D. DiMarchi, R.M. Caprioli, J. M. Spraggins, W.J. Chazin, D.P. Giedroc, E.P. Skaar, Zn-regulated GTPase metalloprotein activator 1 modulates vertebrate zinc homeostasis, Cell 185 (2022) 2148–2163.e27, https://doi.org/10.1016/j.cell.2022.04.011.

[14] W. Qiao, D. Pan, Y. Zheng, S. Wu, X. Liu, Z. Chen, M. Wan, S. Feng, K.M.C. Cheung, K.W.K. Yeung, X. Cao, Divalent metal cations stimulate skeleton interoception for new bone formation in mouse injury models, Nat. Commun. 13 (2022) 535, https://doi.org/10.1038/s41467-022-28203-0.

[15] W. Qiao, H. Xie, J. Fang, J. Shen, W. Li, D. Shen, J. Wu, S. Wu, X. Liu, Y. Zheng, K. M.C. Cheung, K.W.K. Yeung, Sequential activation of heterogeneous macrophage phenotypes is essential for biomaterials-induced bone regeneration, Biomaterials 276 (2021) 121038, https://doi.org/10.1016/j.biomaterials.2021.121038.

[16] H. Takayanagi, Osteoimmunology: shared mechanisms and crosstalk between the immune and bone systems, Nat. Rev. Immunol. 7 (2007) 292–304, https://doi.org/10.1038/nri2062.

[17] Z. Chen, T. Klein, R.Z. Murray, R. Crawford, J. Chang, C. Wu, Y. Xiao, Osteoimmunomodulation for the development of advanced bone biomaterials, Mater. Today 19 (2016) 304–321, https://doi.org/10.1016/j.mattod.2015.11.004.

[18] M. Tsukasaki, H. Takayanagi, Osteoimmunology: evolving concepts in bone–immune interactions in health and disease, Nat. Rev. Immunol. 19 (2019) 626–642, https://doi.org/10.1038/s41577-019-0178-8.

[19] M.C. Walsh, N. Takegahara, H. Kim, Y. Choi, Updating osteoimmunology: regulation of bone cells by innate and adaptive immunity, Nat. Rev. Rheumatol. 14 (2018) 146–156, https://doi.org/10.1038/nrrheum.2017.213.

[20] G.N. Duda, S. Geissler, S. Checa, S. Tsitsilonis, A. Petersen, K. Schmidt-Bleek, The decisive early phase of bone regeneration, Nat. Rev. Rheumatol. 19 (2023) 78–95, https://doi.org/10.1038/s41584-022-00887-0.

[21] Y. Yang, C. He, E. Dianyu, W. Yang, F. Qi, D. Xie, L. Shen, S. Peng, C. Shuai, Mg bone implant: features, developments and perspectives, Mater. Des. 185 (2020) 108259, https://doi.org/10.1016/j.matdes.2019.108259.

[22] C. Nich, Y. Takakubo, J. Pajarinen, M. Ainola, A. Salem, T. Sillat, A.J. Rao, M. Raska, Y. Tamaki, M. Takagi, Y.T. Konttinen, S.B. Goodman, J. Gallo, Macrophages-key cells in the response to wear debris from joint replacements, J. Biomed. Mater. Res. 101 (2013) 3033–3045, https://doi.org/10.1002/jbm.a.34599.

[23] J. Niu, M. Xiong, X. Guan, J. Zhang, H. Huang, J. Pei, G. Yuan, The in vivo degradation and bone-implant interface of Mg-Nd-Zn-Zr alloy screws: 18 months post-operation results, Corros. Sci. 113 (2016) 183–187, https://doi.org/10.1016/j.corsci.2016.10.009.

[24] W. Li, W. Qiao, X. Liu, D. Bian, D. Shen, Y. Zheng, J. Wu, K.Y.H. Kwan, T.M. Wong, K.M.C. Cheung, K.W.K. Yeung, Biomimicking bone–implant interface facilitates the bioadaption of a new degradable magnesium alloy to the bone tissue microenvironment, Adv. Sci. 8 (2021), https://doi.org/10.1002/advs.202102035.

[25] W. Li, W. Qiao, X. Liu, D. Bian, D. Shen, Y. Zheng, J. Wu, K.Y.H. Kwan, T.M. Wong, K.M.C. Cheung, K.W.K. Yeung, Biomimicking bone–implant interface facilitates the bioadaption of a new degradable magnesium alloy to the bone tissue microenvironment, Adv. Sci. 8 (2021), https://doi.org/10.1002/advs.202102035.

[26] H. Yang, B. Jia, Z. Zhang, X. Qu, G. Li, W. Lin, D. Zhu, K. Dai, Y. Zheng, Alloying design of biodegradable zinc as promising bone implants for load-bearing applications, Nat. Commun. 11 (2020) 401, https://doi.org/10.1038/s41467-019-14153-7.

[27] A. Hightower, C.C. Ahn, B. Fultz, P. Rez, Electron energy-loss spectrometry on lithiated graphite, Appl. Phys. Lett. 77 (2000) 238–240, https://doi.org/10.1063/1.126936.

[28] R.A. Vilá, D.T. Boyle, A. Dai, W. Zhang, P. Sayavong, Y. Ye, Y. Yang, J.A. Dionne, Y. Cui, LiH formation and its impact on li batteries revealed by cryogenic electron microscopy, Sci. Adv. 9 (2023), https://doi.org/10.1126/sciadv.adf3609.

[29] F.C. Castro, V.P. Dravid, Characterization of lithium ion battery materials with valence electron energy-loss spectroscopy, Microsc. Microanal. 24 (2018) 214–220, https://doi.org/10.1017/S1431927618000302.

[30] K. Widder, M. Knupfer, O. Knauff, J. Fink, Plasmon behavior of Zn from electron-energy-loss spectroscopy, Phys. Rev. B 56 (1997) 10154–10160, https://doi.org/10.1103/PhysRevB.56.10154.

[31] M. Alda, Lithium in the treatment of bipolar disorder: pharmacology and pharmacogenetics, Mol. Psychiatr. 20 (2015) 661–670, https://doi.org/10.1038/mp.2015.4.

[32] Z. Li, Z.Z. Shi, Y. Hao, H.F. Li, H.J. Zhang, X.F. Liu, L.N. Wang, Insight into role and mechanism of li on the key aspects of biodegradable Zn-Li alloys: microstructure evolution, mechanical properties, corrosion behavior and cytotoxicity, Mater. Sci. Eng. C 114 (2020) 111049, https://doi.org/10.1016/j.msec.2020.111049.

[33] H. Yang, D. Jin, J. Rao, J. Shi, G. Li, C. Wang, K. Yan, J. Bai, G. Bao, M. Yin, Y. Zheng, Lithium-induced optimization mechanism for an ultrathin-strut biodegradable zn-based vascular scaffold, Adv. Mater. 35 (2023), https://doi.org/10.1002/adma.202301074.

[34] R. Pies, Have we undersold lithium for bipolar disorder? J. Clin. Psychopharmacol. 22 (2002) 445–449, https://doi.org/10.1097/00004714-200210000-00001.

[35] L. Chen, C. Deng, J. Li, Q. Yao, J. Chang, L. Wang, C. Wu, 3D printing of a lithium-calcium-silicate crystal bioscaffold with dual bioactivities for osteochondral interface reconstruction, Biomaterials 196 (2019) 138–150, https://doi.org/10.1016/j.biomaterials.2018.04.005.

[36] P. Vestergaard, L. Rejnmark, L. Mosekilde, Reduced relative risk of fractures among users of lithium, Calcif. Tissue Int. 77 (2005) 1–8, https://doi.org/10.1007/s00223-004-0258-y.

[37] N. Kurgan, K.N. Bott, W.E. Helmeczi, B.D. Roy, I.D. Brindle, P. Klentrou, V. A. Fajardo, Low dose lithium supplementation activates Wnt/β-catenin signalling and increases bone OPG/RANKL ratio in mice, Biochem. Biophys. Res. Commun. 511 (2019) 394–397, https://doi.org/10.1016/j.bbrc.2019.02.066.

[38] L. Li, X. Peng, Y. Qin, R. Wang, J. Tang, X. Cui, T. Wang, W. Liu, H. Pan, B. Li, Acceleration of bone regeneration by activating Wnt/β-catenin signalling pathway via lithium released from lithium chloride/calcium phosphate cement in osteoporosis, Sci. Rep. 7 (2017) 1–12, https://doi.org/10.1038/srep45204.

[39] Z. Wu, J. Bai, G. Ge, T. Wang, S. Feng, Q. Ma, X. Liang, W. Li, W. Zhang, Y. Xu, K. Guo, W. Cui, G. Zha, D. Geng, Regulating macrophage polarization in high glucose microenvironment using lithium-modified bioglass-hydrogel for diabetic bone regeneration, Adv. Healthcare Mater. 11 (2022), https://doi.org/10.1002/adhm.202200298.

[40] L. Huang, X. Yin, J. Chen, R. Liu, X. Xiao, Z. Hu, Y. He, S. Zou, Lithium chloride promotes osteogenesis and suppresses apoptosis during orthodontic tooth movement in osteoporotic model via regulating autophagy, Bioact. Mater. 6 (2021) 3074–3084, https://doi.org/10.1016/j.bioactmat.2021.02.015.

[41] A. Nassar, A.N. Azab, Effects of lithium on inflammation, ACS Chem. Neurosci. 5 (2014) 451–458, https://doi.org/10.1021/cn500038f.

[42] R. Hu, J. Qin, W. Feng, X. Song, H. Huang, C. Dai, B. Zhang, Y. Chen, Lysosomal zinc nanomodulation blocks macrophage pyroptosis for counteracting atherosclerosis progression, Sci. Adv. 11 (2025), https://doi.org/10.1126/sciadv.adu3919.

[43] Y. Wu, S. Zhu, C. Wu, P. Lu, C. Hu, S. Xiong, J. Chang, B.C. Heng, Y. Xiao, H. W. Ouyang, A bi-lineage conducive scaffold for osteochondral defect regeneration, Adv. Funct. Mater. 24 (2014) 4473–4483, https://doi.org/10.1002/adfm.201304304.

[44] T.L. Lin, Y.H. Lin, A.K.X. Lee, T.Y. Kuo, C.Y. Chen, K.H. Chen, Y.T. Chou, Y. W. Chen, M.Y. Shie, The exosomal secretomes of mesenchymal stem cells extracted via 3D-printed lithium-doped calcium silicate scaffolds promote osteochondral regeneration, Mater. Today Bio 22 (2023) 100728, https://doi.org/10.1016/j.mtbio.2023.100728.

[45] N. Li, J. Bai, W. Wang, X. Liang, W. Zhang, W. Li, L. Lu, L. Xiao, Y. Xu, Z. Wang, C. Zhu, J. Zhou, D. Geng, Facile and versatile surface functional polyetheretherketone with enhanced bacteriostasis and osseointegrative capability for implant application, ACS Appl. Mater. Interfaces 13 (2021) 59731–59746, https://doi.org/10.1021/acsami.1c19834.

[46] M.-C. Vantyghem, Iatrogenic endocrine complications of lithium therapy, Ann. Endocrinol. 84 (2023) 391–397, https://doi.org/10.1016/j.ando.2023.03.004.

[47] L.A. Córdova, F. Loi, T.-H. Lin, E. Gibon, J. Pajarinen, A. Nabeshima, L. Lu, Z. Yao, S.B. Goodman, CCL2, CCL5, and IGF-1 participate in the immunomodulation of osteogenesis during M1/M2 transition in vitro, J. Biomed. Mater. Res. 105 (2017) 3069–3076, https://doi.org/10.1002/jbm.a.36166.

[48] K. Wintges, F.T. Beil, J. Albers, A. Jeschke, M. Schweizer, B. Claass, G. Tiegs, M. Amling, T. Schinke, Impaired bone formation and increased osteoclastogenesis in mice lacking chemokine (C-C motif) ligand 5 (Ccl5), J. Bone Miner. Res. 28 (2013) 2070–2080, https://doi.org/10.1002/jbmr.1937.

[49] Y. Liu, Y. Kao, W. Huang, K. Lin, S. Wu, S. Hsu, S.C. Schuyler, L. Li, F. Leigh Lu, J. Lu, CCL5/RANTES is important for inducing osteogenesis of human mesenchymal stem cells and is regulated by dexamethasone, Biosci. Trends 8 (2014) 138–143, https://doi.org/10.5582/bst.2014.01047.

[50] W. Qiao, K.H.M. Wong, J. Shen, W. Wang, J. Wu, J. Li, Z. Lin, Z. Chen, J. P. Matinlinna, Y. Zheng, S. Wu, X. Liu, K.P. Lai, Z. Chen, Y.W. Lam, K.M.C. Cheung, K.W.K. Yeung, TRPM7 kinase-mediated immunomodulation in macrophage plays a central role in magnesium ion-induced bone regeneration, Nat. Commun. 12 (2021) 2885, https://doi.org/10.1038/s41467-021-23005-2.

[51] C.E. Repeke, S.B. Ferreira, M. Claudino, E.M. Silveira, G.F. de Assis, M.J. Avila-Campos, J.S. Silva, G.P. Garlet, Evidences of the cooperative role of the chemokines CCL3, CCL4 and CCL5 and its receptors CCR1+ and CCR5+ in RANKL+ cell migration throughout experimental periodontitis in mice, Bone 46 (2010) 1122–1130, https://doi.org/10.1016/j.bone.2009.12.030.

[52] J.-W. Lee, A. Hoshino, K. Inoue, T. Saitou, S. Uehara, Y. Kobayashi, S. Ueha, K. Matsushima, A. Yamaguchi, Y. Imai, T. Iimura, The HIV co-receptor CCR5 regulates osteoclast function, Nat. Commun. 8 (2017) 2226, https://doi.org/10.1038/s41467-017-02368-5.

[53] I. Andrade, S.R.A. Taddei, G.P. Garlet, T.P. Garlet, A.L. Teixeira, T.A. Silva, M. M. Teixeira, CCR5 down-regulates osteoclast function in orthodontic tooth movement, J. Dent. Res. 88 (2009) 1037–1041, https://doi.org/10.1177/0022034509346230.

[54] S. Yano, R. Mentaverri, D. Kanuparthi, S. Bandyopadhyay, A. Rivera, E.M. Brown, N. Chattopadhyay, Functional expression of β-chemokine receptors in osteoblasts: role of regulated upon activation, normal T cell expressed and secreted (RANTES) in osteoblasts and regulation of its secretion by osteoblasts and osteoclasts, Endocrinology 146 (2005) 2324–2335, https://doi.org/10.1210/en.2005-0065.

[55] M. Zhang, E. Liu, X. Xiao, S. Yu, H. Li, K. Wang, P. Gong, W. Li, Y. Song, D. Sun, Z. Li, Microstructure, mechanical properties and in vitro degradation properties of Zn-Fe alloys, Mater. Char. 192 (2022) 112220, https://doi.org/10.1016/j.matchar.2022.112220.

[56] R. Yue, H. Huang, G. Ke, H. Zhang, J. Pei, G. Xue, G. Yuan, Microstructure, mechanical properties and in vitro degradation behavior of novel Zn-Cu-Fe alloys, Mater. Char. 134 (2017) 114–122, https://doi.org/10.1016/j.matchar.2017.10.015.

[57] H. Yang, B. Jia, Z. Zhang, X. Qu, G. Li, W. Lin, D. Zhu, K. Dai, Y. Zheng, Alloying design of biodegradable zinc as promising bone implants for load-bearing applications, Nat. Commun. 11 (2020) 401, https://doi.org/10.1038/s41467-019-14153-7.

[58] X. Tong, Y. Tong, J. Zheng, R. Shi, H. Liang, M. Li, Y. Meng, J. Shi, D. Zhao, C. R. Seehus, J. Wang, X. Xu, T. Boczek, S. Suzuki, A. Fleig, R. Penner, N. Zhang, J. Xu, J. Duan, Z. Yu, W. Wang, W. Zhao, F. Guo, TRPM7 contributes to pyroptosis and its involvement in status epilepticus, J. Neuroinflammation 21 (2024) 315, https://doi.org/10.1186/s12974-024-03292-4.

[59] M. Li, T. Wei, H. Liu, Z. Wu, J. Zhou, J. Jiang, P. He, Y. Zhang, Y. Zheng, Revolutionizing bone tumor therapy: biodegradable magnesium implant triggers cGAS-STING-Dependent synergy of autophagic cell death and alkaline metabolic collapse, Adv. Funct. Mater. (2025), https://doi.org/10.1002/adfm.202507822.

[60] W. Qiao, D. Pan, Y. Zheng, S. Wu, X. Liu, Z. Chen, M. Wan, S. Feng, K.M.C. Cheung, K.W.K. Yeung, X. Cao, Divalent metal cations stimulate skeleton interoception for new bone formation in mouse injury models, Nat. Commun. 13 (2022) 535, https://doi.org/10.1038/s41467-022-28203-0.

[61] T.E. Lockwood, M.T. Westerhausen, P.A. Doble, Pew2: open-source imaging software for laser ablation-inductively coupled plasma-mass spectrometry, Anal. Chem. 93 (2021) 10418–10423, https://doi.org/10.1021/acs.analchem.1c02138.